DOKUZ EYLÜL UNIVERSITY
GRADUATE SCHOOL OF NATURAL AND APPLIED SCIENCES

VOLTAGE CONTROLLED PHOTOVOLTAIC PUMPING SYSTEM WITH A BRUSHLESS DC MOTOR (BLDC)

by
Tafadzwa MUGWAMBA

March, 2020
İZMİR

VOLTAGE CONTROLLED PHOTOVOLTAIC PUMPING SYSTEM WITH A BRUSHLESS DC MOTOR (BLDC)

A Thesis Submitted to the
Graduate School of Natural And Applied Sciences of Dokuz Eylül University
In Partial Fulfillment of the Requirements for the Master of
Electrical and Electronics Engineering Program

by
Tafadzwa MUGWAMBA

March, 2020
İZMİR

M.Sc THESIS EXAMINATION RESULT FORM

We have read the thesis entitled "**VOLTAGE CONTROLLED PHOTOVOLTAIC PUMPING SYSTEM WITH A BRUSHLESS DC MOTOR (BLDC)**" completed by **TAFADZWA MUGWAMBA** under supervision of **PROF. DR. EYUP AKPINAR** and we certify that in our opinion it is fully adequate, in scope and in quality, as a thesis for the degree of Master of Science.

....

Prof. Dr. Eyup AKPINAR

Supervisor

....	....
Assoc. Prof. Dr. Özge CİHANBEĞENDİ	Assoc. Prof. Dr. Mutlu BOZTEPE
Jury Member	Jury Member

Prof. Dr. Kadriye ERTEKİN
Director
Graduate School of Natural and Applied Sciences

ACKNOWLEDGEMENTS

Firstly, I would like to express my sincere gratitude to my supervisor Prof. Dr. Eyup AKPINAR for his invaluable support and patience throughout the course of my masters studies, for his willingness and commitment to continuosly educate and share with me his vast knowledge. It has been an honor for me to be his student.

I would also like to thank other professors and members of the Department of Electrical and Electronics Engineering who have had a role to play in the advancement of my academic career.

I would like to thank the Turkish Ministry of Culture and Tourism for the scholarship award that opened the doors for my graduate studies and their support throughout the whole period.

Special gratitude goes to my family, to whom I dedicate this achievement, my mother Chenai, my father Simon and my sibilings, for they are my pillar of strength in all times.

Tafadzwa MUGWAMBA

VOLTAGE CONTROLLED PHOTOVOLTAIC PUMPING SYSTEM WITH A BRUSHLESS DC MOTOR (BLDC)

ABSTRACT

Many developments have taken place in the field of renewable energy over the past decade, with a large percentage of research activities being oriented towards solar energy. We have seen the rise of grid connected photovoltaic systems as well as standalone PV systems. Standalone systems have gained vast implementation in remote locations where the grid is unavailable for applications such as irrigation schemes in domestic applications, however, unlike grid connected systems that are linked with the network bus voltage, standalone solar systems present undesirable complications in terms of stability. This thesis seeks to address this problem by developing and investigating a proposed optimal design of standalone photovoltaic pumping system. This study has made use of the brushless DC motor (BLDC) which has over the years proven to be a good substitute to the traditional brushed DC motors and the induction motors. The aim was to solve the problem of controllability of the pump speed while utilizing the maximum possible power from the PV array. This thesis proposed a two-stage PV system comprising of a primary DC stage for maximum power point tracking and a secondary AC stage dedicated for voltage regulation. For the DC stage, a Buck-Boost converter was used and for the AC stage, a full H bridge inverter was utilized.

Keywords: Photovoltaic, Brushless DC motor,Two-stage system, Maximum Power Point Tracking, DC-DC converter, Inverter

FIRÇASIZ DOĞRU AKIM MOTORU İLE GERİLİM KONTROLLÜ FOTOVOLTAİK POMPA SİSTEMİ

ÖZ

Son yıllarda yenilenebilir enerji alanında birçok gelişme meydana gelmiştir ve araştırma faaliyetlerinin büyük bir kısmı güneş enerjisine yöneliktir. Şebekeye bağlı fotovoltaik sistemlerin ve bağımsız PV sistemlerinin yükselişini gördük. Bağımsız sistemler, şebekenin ev içi uygulamalardaki sulama şemaları gibi uygulamalar için kullanılamadığı uzak yerlerde büyük bir uygulama kazanmıştır, ancak şebeke ile bağlantılı sistemlerin aksine, bağımsız güneş sistemleri kararlılık açısından istenmeyen komplikasyonlar sunmaktadır. Bu tez, bağımsız fotovoltaik pompalama sisteminin önerilen optimum tasarımını geliştirerek ve araştırarak bu sorunu ele almayı amaçlamaktadır. Bu çalışma, yıllar boyunca fırçalı DC motorlara ve endüksiyon motorlarına iyi bir alternatif olduğu kanıtlanmış fırçasız DC motoru (BLDC) kullanmıştır. Amaç, PV dizisinden mümkün olan maksimum gücü kullanırken pompa hızının kontrol edilebilirliği problemini çözmekti. Bu tez, maksimum güç noktası takibi için bir birincil DC aşaması ve voltaj regülasyonu için ayrılmış bir ikincil AC aşaması içeren iki aşamalı bir PV sistemi önerdi. DC kademesi için bir Buck-Boost konvertörü kullanıldı ve AC kademesi için tam bir H köprü invertörü kullanıldı.

Anahtar kelimeler: Fotovoltaik, Fırçasız DC motor, İki aşamalı sistem, Maksimum Güç Noktası İzleme, DC-DC dönüştürücü, İnvertör

CONTENTS

LIST OF FIGURES

Page

LIST OF TABLES

CHAPTER ONE
INTRODUCTION

Due to the abrupt increase in global energy demand coupled with the growing concerns over climate change and the state of the environment in most parts of the world because of the excess carbon dioxide emissions into the atmosphere, the energy sector faces the difficult task of meeting this great energy need while attempting to avoid the risk of putting our livelihood at danger. To put this into perspective, most governments across the globe, have taken up a sustainable development agenda as part of their long-term administrative goal. The Paris Agreement (IRENA, 2019) is a good example of all the world endeavours to move towards having cleaner and safer environments. This agreement aims to have carbon dioxide emissions reduced by an average of 3.5% per year up until the year 2050. At the forefront of this agenda is the replacement of traditional fossil fuels with unconventional, reliable, and environmentally friendly energy sources. Amongst these, are renewable energy sources such as wind and solar have engrossed more attention as the most suitable solution to this crisis. This position can be attributed to the accessibility, cleanliness and low maintenance requirement of such energy sources. While wind energy has proven to be an appropriate substitute, solar energy over the past few years has been edging closer to having almost the same impact as that of wind energy, drawing way more attention from scientists and engineers as a more viable energy source for the future, mostly because of the major developments that have taken place in the semiconductor industry and have paved way for the production of cheaper, more advanced solar cells that exhibit efficiencies several times higher than what existed before.

By the year 2018, the global installed solar capacity was around 480 GW, of which 2.94 GW were off grid PV systems, having increased from a mere 0.25 GW in 2008. If the world continues to move along the same roadmap, it is expected that by the year 2050 wind energy will constitute around 30% of the world's total electricity generation sources and solar energy will constitute around 25% (IRENA, 2019).

Given the infinite nature of the energy available from the sun, photovoltaic (PV) systems present us with endless possibilities in regard to how much power we can retrieve. As a result, many researchers have put an extensive amount of time and effort into studying and developing solar systems for both grid tied and standalone applications. However, in doing so, the research pool has been flooded by a large number of conceptualized novel designs of PV systems that are more focused on the modification of previous topologies, leaving behind a lot of questions regarding best practice when it comes to the design of such systems for specific applications. It is up to the researcher to bring to light the advantages and disadvantages of the various techniques and topologies commonly used in solar photovoltaic systems. While solar PV systems are in use in various area today, one field in which they have found significant importance and is the motivation to this research is that of isolated solar water supply.

Pumping systems are important for many purposes ranging from domestic to industrial and particularly important for irrigation schemes in farming regions. Standalone Solar Photovoltaic (PV) pumping systems have widely become the preferred choice for water supply, particularly in non-urban regions where access to national grids is generally limited. The technology enables the inhabitants of such regions to benefit from the significant amount of solar radiation available to them during the seasons of the year when irradiance levels are favourable. The majority of the PV pumping systems that are installed are currently running low energy pumps and are commonly utilized in domestic and small scale irrigation schemes. An estimated number of about 100,000 solar pumping systems have been built worldwide to date, and all comprising of varying system components and configurations. Additionally, the potential for the use of solar powered pumping systems for large scale irrigation schemes has been seen to be on the rise.

Although there are several different types of water pumps available on the market, the two most commonly used types of pumps on the centrifugal pump and the positive displacement pump. In the case of the positive displacement pump, the output of water is directly proportional to the rotational speed of the pump independent of the pumping head. These are used for solar water pumping from boreholes and deep wells. Centrifugal pumps on the other hand are usually used for low head applications, particularly when directly connected to solar PV arrays. Centrifugal pumps usually come in fixed head designs, while the pressure produced by the pump is directly proportional to the rotational speed. As compared to the positive displacement pumps, centrifugal pumps have relatively higher efficiencies and are capable of pumping larger volumes of water (Chandrasekaran, 2012). These are usually used in conjunction with an electric motor.

The majority of installed pumps typically use a brushed permanent magnet motor although some studies have also been carried out on the use of other motors, such as the shunt and separately excited motors. Induction motors have also shown to be a reliable solution, particularly in borehole and deep pumping applications due to their having minimum maintenance requirements. Recently, the BLDC motor has grown to become preferred type of motor for this application for several reasons (see Table 1.1). BLDC motors are gaining a lot of momentum as the long-term viable replacement for brushed DC motors and induction motors as they present both equipment designers and users with better options when it comes to weight, efficiency and durability. Brushless DC motors are capable of offering the same performance characteristics as DC permanent magnet motors without the need of having brushes which are usually subject to wearing and also cause sparks in the motor. The BLDC motors also have additional advantages over the traditional DC motors and induction motors such as higher speed and low noise operation. From Table 1.1 it can be seen that the brushless DC motor overall outperforms both the brushed DC motors and induction motors, however this comes at an extra cost which can also be considered as a long-term investment given the low maintenance requirements of this motor.

The potential for BLDC motors to become the main motor type for different applications across all industries in the future is high, but in the case of operation of this type of motor for a pump drive in conjunction with the PV system without a battery set, there are some factors to be taken into account in order to achieve controlled operation of the pump. The speed of the motor is directly proportional to

Table 1.1 Comparison between BLDC motors, Brushed DC motors and Induction motors

Characteristic	Brushed DC Motors	Induction Motors	Brushless DC Motors
Mechanical Structure	The field magnets on the stator and rotor are permanent magnets or electromagnets	Both stator and rotor have windings.	The field magnets on the rotor and the are stator permanent magnets
Speed/Torque Characteristics	Moderate. Losses in brushes reduce torque at higher speeds.	Nonlinear	Flat. Operates at all speeds with rated load.
Dynamic response	Slow	Slow	Fast – is a lower rotor inertia because of permanent magnets
Lifetime/ Maintenance	Short. Regular maintenance required because of brushes.	Average. Low maintenance	Long – requires minimum to no maintenance: no brushes or commutator
Efficiency	Moderate. Losses in brushes.	Low. Current losses in both stator and rotor.	High. No losses in brushes.
Commutation Method	Mechanical. Contact between brushes and commutator.	Requires starting mechanism.	Electronic. Uses solid-state switches.
Speed Range	Moderate. Losses in brushes	Low. Dependent on AC line frequency and Load.	High. No losses in brushes
EMI Noise	High. Due to losses in brushes.	Low.	Low.
Rotor Position Sensing	Automatic. Done by brushes and commutator	None	Hall sensors, optical encoders etc.
Reverse Operation	By reversing the polarity of the terminal voltage.	Phase shift.	By reversing the switching sequence.
Controller Requirements	Controller only required for variable speed operation.	Controller only required for variable speed operation.	Controller is always needed for commutation.

the input voltage at the terminals of the BLDC motor drive, but for a directly connected solar powered pumping system speed control becomes compromised since the voltage generated by the PV array is proportional to the irradiance, which in is continuously varying during the day. Unfortunately, most commercially installed PV pumping system operate with this setup and in that case the system operates at the intersection of the current voltage curve of the PV array which may not be the maximum power point (MPP). In order to improve the efficiency of the PV system it is common practice to implement a maximum Power point tracking algorithm, which is done by connecting a DC-DC converter at the output of the PV array as an interface between the PV source and the motor, and using a control device to adjust the duty cycle of the converter, altering the voltage and current values in such a way that the maximum power is extracted from the solar panel. Although the overall efficiency of the system is significantly increased, the output voltage of the DC to DC converter is not controlled. For a directly connected pumping system, this operation essentially means that the MPPT controller, controls the armature voltage of the motor, and thus the rotational speed of the pump. From this, it can be seen that with or without a maximum Power point tracking algorithm, speed control remains compromised because of the varying input voltage. (Elgendy, 2013) proposes a constant voltage MPPT algorithm to increase their efficiency of PV systems by constantly operating them at the voltage level corresponding to the maximum Power point.

The AC input BLDC motor drive considered in this study is equipped with an integrated rectifier circuit, allowing the drive to be fed directly from sources supplying voltages similar to grid voltage. As such, this thesis proposes a two-stage PV system consisting of a primary DC stage comprised of the PV array and a DC to DC converter operating with a Maximum Power Point Tracking (MPPT) algorithm and a secondary AC stage comprised of a Single Phase Voltage Source Inverter (VSI). With this set up, the system is capable of extracting the maximum power from the PV array by the operation of the DC-DC converter while regulating the voltage level using the DC-AC inverter which in turn feeds the AC input BLDC motor drive which then runs the centrifugal pump.

Some researchers who have used approaches somewhat similar to what is proposed in this thesis include (Scortegagna, 2019), who also explore multistage solar PV pumping systems. In other studies (Kumar, 2016) explores this same idea using different converter topologies directly connected to the PV array, as well as operation using a battery (Kumar, 2014). Other researchers such as (Salem, 2015) have made use of a two-stage PV system for grid connected applications to help enhance power quality by minimizing the double grid frequency voltage ripple that affects the DC link voltage in single phase grid connected PV units.

The rest of the thesis is organized as follows: Chapter 2 describes the two-stage standalone photovoltaic pumping system, its components and applicable techniques. Chapter 3 consists of the system design and analysis. Chapter 4 contains simulation results. In chapter 5 conclusions are drawn regarding the proposed system.

CHAPTER TWO
TWO-STAGE STAND-ALONE PHOTOVOLTAIC PUMPING SYSTEM

This chapter presents an overview of the system proposed in this thesis, its components and a review of the related methods and techniques applicable to the design of such a system. The structure of the proposed two-stage solar PV system is depicted in figure 2.1.

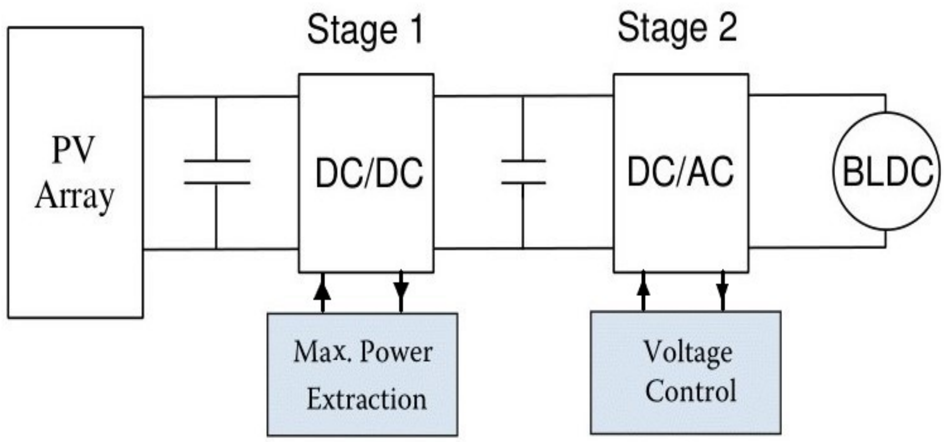

Figure 2.1 Proposed two-stage PV system

The first stage of the system comprises of the DC-DC buck boost converter in conjunction with the PV array to form a DC generator operating with the maximum power point tracking algorithm. The second stage of the system comprises of a single phase full bridge voltage source inverter in conjunction with an LCL filter. The two stages are connected via a DC link capacitor in order to reduce the DC voltage ripple. The LCL filtered VSI is controlled in a closed-loop by a voltage oriented controller to output the sinusoidal waveform that feeds the AC input to the BLDC motor drive to run the pump. This set up does not include a battery, as such in order to achieve continuous operation of the system in different conditions, the correct sizing of the PV array is important.

2.1 The PV Module

Solar PV arrays are capable of powering various types of loads by their ability to convert sunlight into electrical energy. The output current and voltage at the terminals of the array are directly dependent on the amount of solar irradiation present, as well as the temperature of the solar cells. The equivalent circuit of a solar cell is shown in figure 2.2.

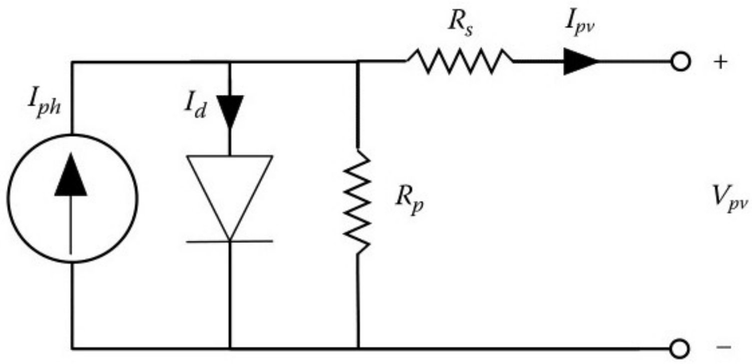

Figure 2.2 Equivalent circuit of a solar cell

Rs and Rp are the series and shunt resistances of the cell and Id is the saturation current. The voltage are current produced by a solar cell depend on temperature and irradiance. The I-V and P-V characteristics of PV cells are non linear.

2.1.1 Characteristics of the PV module

Figure 2.3 shows the variation of the I-V characteristic of a typical PV cell with changes in temperature where T1 is the normalized temperature, which is less than T2 - which is less than T3 and so on.

Figure 2.4 shows the variation of the I-V characteristic of a typical PV cell with changes in irradiance where G1 is the normalized temperature, which is greater than G2 - which is greater than G3 and so on.

Figure 2.5 shows the variation of the P-V characteristic of a typical PV cell with

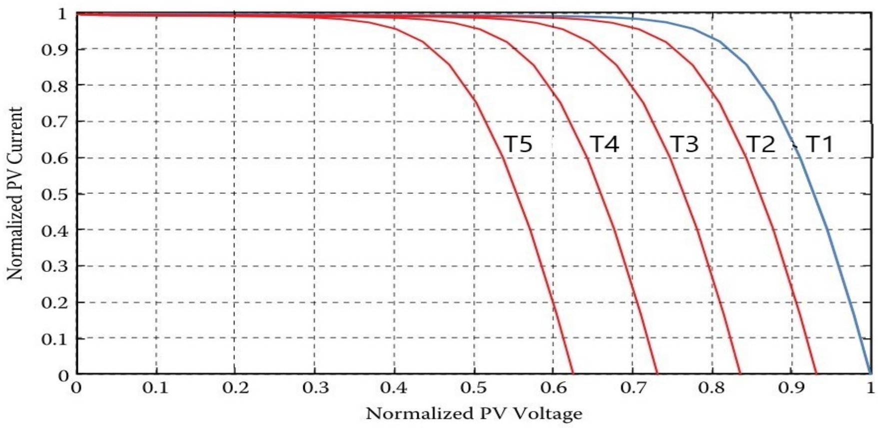

Figure 2.3 Effect of temperature on solar I-V characteristic

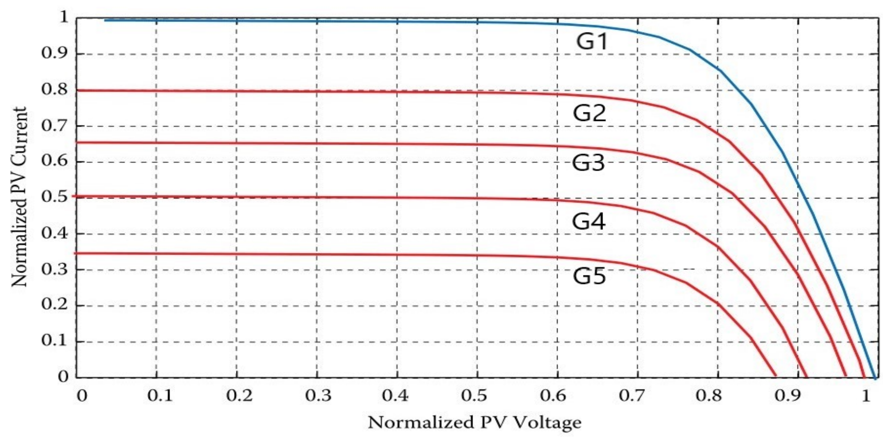

Figure 2.4 Effect of irradiance on solar I-V characteristic

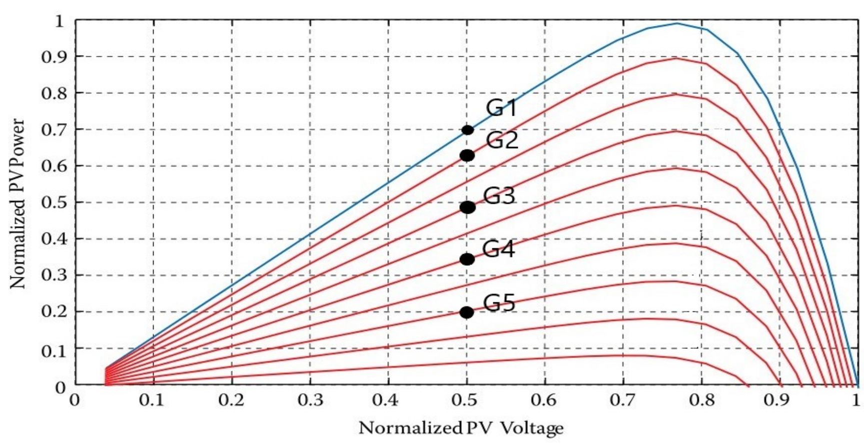

Figure 2.5 Effect of irradiance on solar P-V characteristic

changes in irradiance where G1 is the normalized temperature, which is greater than G2 - which is greater than G3 and so on.

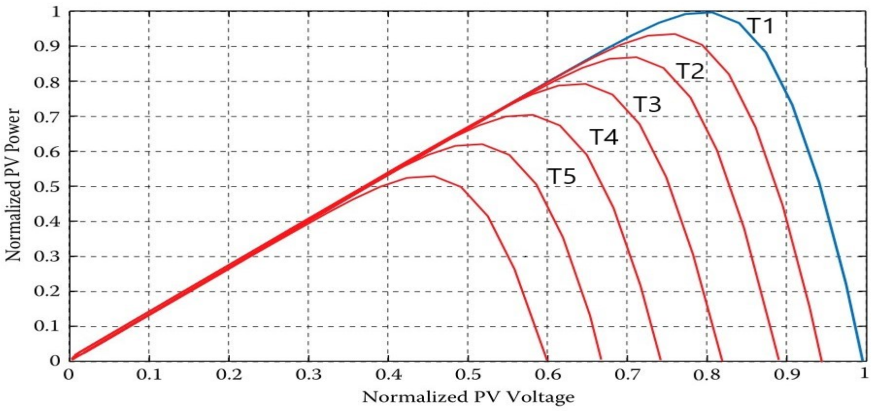

Figure 2.6 Effect of temperature on solar P-V characteristic

Figure 2.6 shows the variation of the P-V characteristic of a typical PV cell with changes in temperature where T1 is the normalized temperature, which is less than T2 - which is less than T3 and so on.

2.2 Maximum Power Point Tracking

Optimal utilization of solar PV systems by means of maximum power point tracking (MPPT remains one of the main topics for many researchers in the field of photovoltaics. Several different methods and strategies for retrieving the maximum amount of power from solar arrays have been presented in literature. The general idea behind MPPT strategies is to control the parameter values of the PV array such that system operates at a particular point of the P – V curve corresponding to the maximum power available at specified levels of irradiance and temperature. In all modern solar systems, this controller is a critical part of the system. This technique is done by adding a converter as an interface linking PV array to the load, and providing a means of parameter regulation through the switching operation of the converter. Besides regulating the current and voltage values of the PV generator, the converter is also used for load matching and power flow control. By regulating either the voltage or the current value at the output terminal of the array, thus adjusting the PV operating point, the intermediate converter is used to track the maximum power point (MPP) of the solar PV array in an attempt to extract the maximum possible power available at that time. The most commonly used type of converters in PV interfacing and the implementation of the MPPT algorithm are DC-DC converters.

The most commonly used MPPT algorithm is the perturb and observe algorithm because of its effectiveness and simplicity in implementation. The incremental conductance algorithm (Hosseini, 2013) is yet another algorithm that has gained widespread implementation. Some authors have focused on other ‘’non-standard” maximum power point tracking methods such as fuzzy logic, artificial neural networks , while others have dedicated their work to developing advanced, highly responsive and more efficient versions of the old aged perturb and observe MPPT algorithm (Femia, 2005). (Jubaer, 2018) proposes an enhanced adaptive perturb and observe maximum power point tracking algorithm EA-P&O), aimed at eliminating the steady-state oscillations and improving the global peak tracking capability of the algorithm under partial shading. The author compares this method to other advanced MPPT algorithms such as the modified incremental conductance algorithm (MIC), the artificial bee colony algorithm (ABC), the cuckoo search (CS) algorithm, and the hybrid P&O – Ant Colony Optimization algorithm (ACO-P&O).

It is clear that the choice of the maximum power point tracking algorithm used in a solar PV system is of crucial importance as it affects the overall efficiency of the PV array, and as such, indepth research on this topic is required in order to identify the pros and cons of each method and the possibilities of improvement. However, this aspect is not part of this thesis. For this study, the perturb and observe algorithm in its general form is implemented (Maissa, 2016; Amine, 2013).

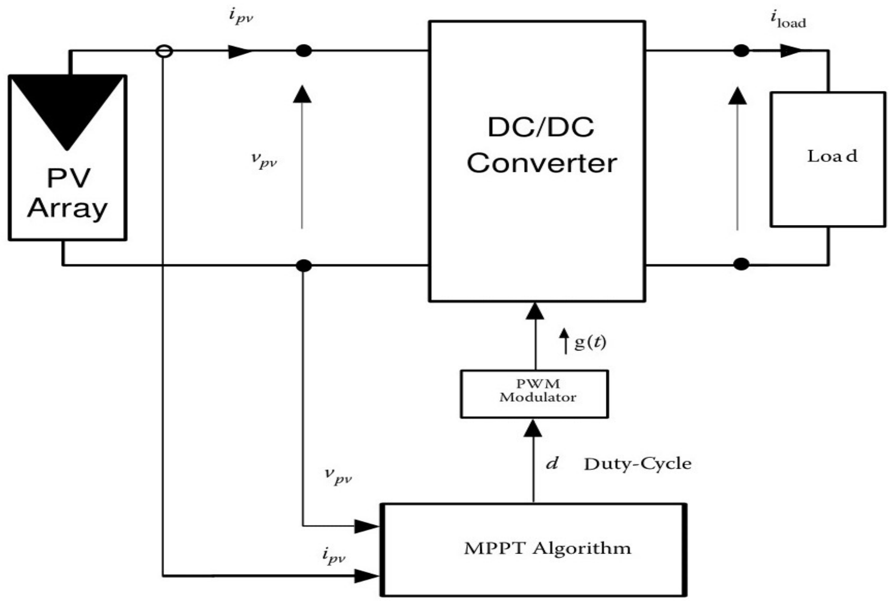

Figure 2.7 Implementation of MPPT

2.2.1 The Perturb and Observe MPPT algorithm

The perturb and observe maximum power point tracking algorithm is the industry's most preferred and widely used method of extracting the maximum available power from the PV array. In literature, three techniques for implementing the P&O algorithm are proposed and these are the reference voltage perturbation method, the current reference perturbation technique (Kakosimos, 2013 and the direct duty cycle perturbation method. In the reference voltage perturbation and current reference perturbation techniques, the output of the MPPT controller is current or voltage reference signal. This reference signal is compared to the actual PV voltage signal and the error processed by a controller such as a PI controller to produce the duty cycle reference which is processed through pulse width modulation to produce the gate signal for the DC-DC converter switch. In the direct duty cycle perturbation method, the output of the MPPT the algorithm is the duty cycle reference, which is directly processed by the pulse width modulation technique to produce the gate signal. The most common approach is that of the voltage based P&O algorithm. The logic behind the operation of this method is simple: the controller obtains the instantaneous values of the PV voltage and current at the output of the array and uses these to calculate the instantaneous power that is in turn compared to the previous value of the power. Depending on whether the power increased or decreased, the duty cycle of the DC-DC converter is adjusted to change the value of the PV voltage in such a way that the operating point moves in a hill climbing manner towards the maximum power point. When the point on the P – V curve corresponding to the maximum Power point is reached the difference between the previous power in the current instantaneous power becomes zero and there is no change in duty cycle. Even if irradiance and temperature are not changing, the MPPT algorithm continues to perturb the operating point of the system causing the PV array terminal voltage to fluctuate around the maximum power point voltage (Elgendy, 2012).

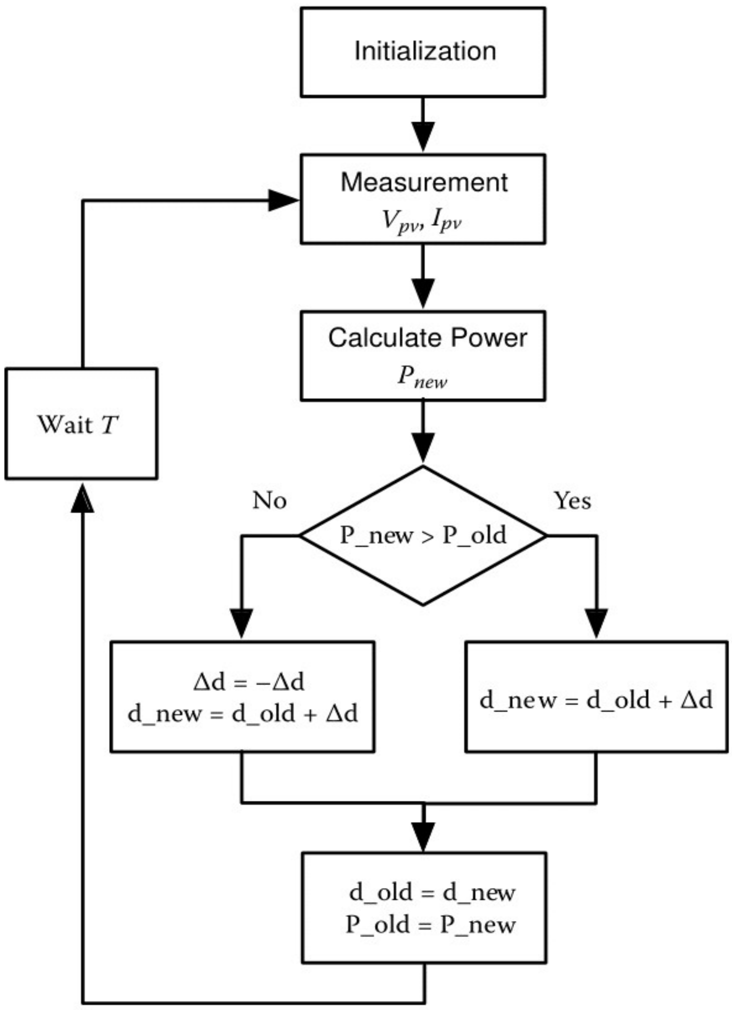

Figure 2.8 Perturb and Observe maximum power point tracking algorithm

The P&O tracking method can be a fixed step size or variable step size algorithm (Guerrero, 2016. The fixed step size perturb and observe algorithm is -

one in which the duty cycle is adjusted by a constant value for every cycle. In the variable step size algorithm, the value by which the duty cycle is adjusted is proportional to the difference in power for the two consecutive cycles. The variable step size algorithm is characterized by shorter convergence time and a low steady-state error. As for the fixed step size algorithm, when this step size is large, the convergence is fast but resulting in a steady-state error, and when the step size is small there is less steady-state error but the convergence is slow.

2.2.2 DC-DC Converter Topologies for MPPT Applications

The DC-DC converter plays an important role in the proposed system as an impedance matching interface between the PV array and the DC to AC inverter and acts to extract the maximum possible power. Selecting the right converter for MPPT applications is important in assuring optimal performance of the photovoltaic system. A poor choice of DC-DC converter may result in overall low system efficiency. The two main considerations in the proposed two-stage standalone PV system are efficiency and overall system stability. In terms of efficiency, the system should be able to extract the maximum possible power from the PV array and in terms of stability the proposed system should be able to maintain normal operation under the dynamic conditions imposed by the action of the MPPT algorithm.

With several DC-DC converters being used interchangeably for the design and implementation of MPPT strategies in solar PV systems both for research purposes and in industry, a question regarding the choice of converter topology best suited for this application arises. For a PV system running a current ,duty cycle or voltage oriented MPPT algorithm, when the level of solar irradiation or temperature changes, the algorithm generates a new parameter reference which disturbs the duty cycle of the converter and thus causing all other parameters to change. As a rule of thumb in engineering, for all dynamic systems the greatest area of concern is stability. A robust PV generator is one that is capable of operation in the stable region regardless of rapid changes occurring. In literature, the buck boost converter is highlighted as one of the converters capable of high-efficiency maximum power point tracking, and can track the maximum power in all regions of operation. In the following sections, the buck, boost and buck-boost converters will be briefly mentioned on the basis of their maximum power point tracking regions.

2.2.2.1 The Buck Converter

The buck converter is a DC to DC converter whose output voltage is lower than the input voltage. This type of converter is also known as the step down converter. The buck converter is commonly used for battery charging and interfacing of PV arrays of higher voltage rating. The buck converter circuit is shown in figure 2.9.

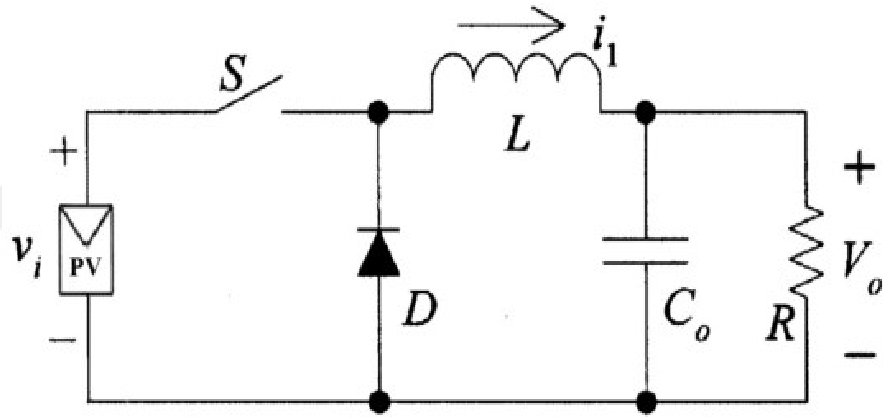

Figure 2.9 Buck converter circuit

In the ON state, the diode is reversed biased, blocking current flow. During this period the current flowing through the inductor arises from its minimal value to the maximum value in the inductor stores up energy. In the OFF state, the energy previously stored in the inductor is transferred to the load and the capacitor, and the inductor current decreases from its maximum value to its minimal value. For successful maximum power point tracking, the controller changes the duty cycle of the converter so as to match the input impedance to the load impedance. The tracking and non-tracking regions of the buck converter in MPPT application are depicted in figure 2.10.

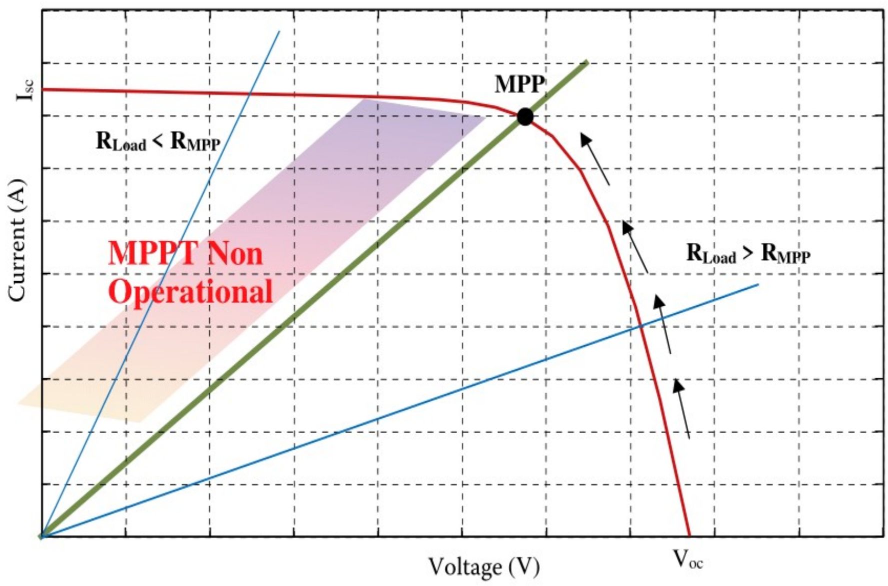

Figure 2.10 Buck converter MPP tracking region

2.2.2.2 The Boost Converter

The boost converter is a DC to DC converter whose output voltage is higher than the input voltage. This type of converter is also known as a step up converter. The boost converter circuit is shown in figure 2.11

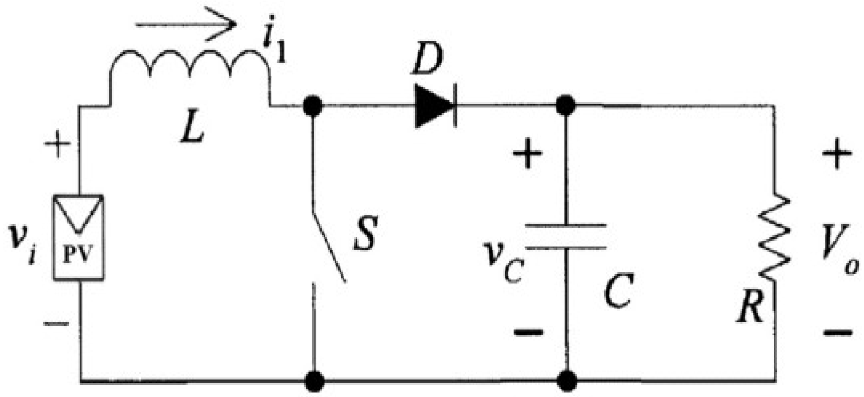

Figure 2.11 Boost converter circuit

In the ON state, current flows through the inductor, rising from its minimal value to its maximum value and the inductor stores energy. During this period, the diode is reversed biased, isolating the load from the source. Continuous current on the load side is maintained by the capacitor. In the OFF state, the total sum of the voltage across the inductor and the source appears at the terminals, giving an overall voltage level higher than the source itself. During this period, the inductor current falls from its maximum value to its minimal value. For successful maximum power point tracking, the controller changes the duty cycle of the converter so as to match the input impedance to the load impedance. The tracking and non-tracking regions of the boost converter in MPPT application are depicted in figure 2.12.

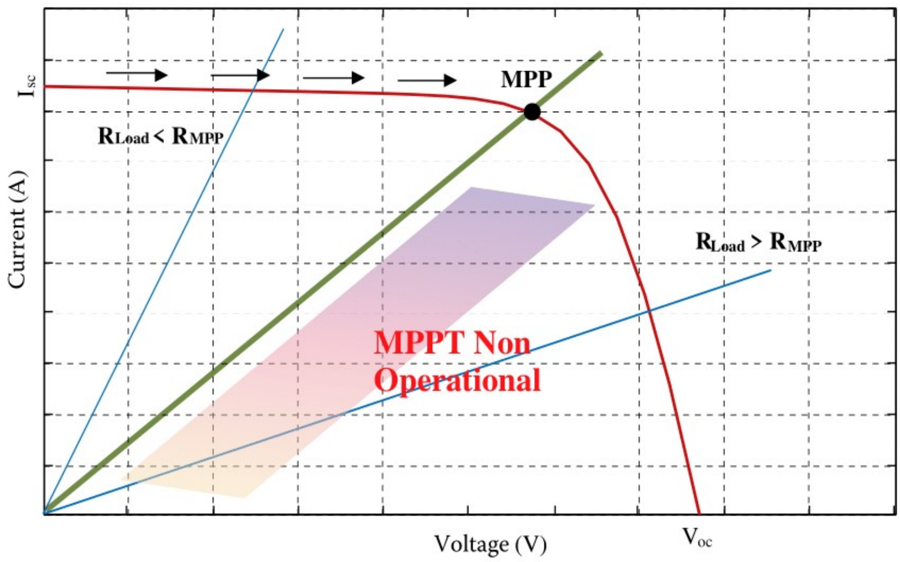

Figure 2.12 Boost converter MPP tracking region

2.2.2.3 The Buck-Boost Converter

This converter has two main topologies, the negative output topology which has one switching device and the positive output topology with 2 switching devices (Narasimharaju, 2015). The inverting type (negetive output) buck boost converter circuit is given in figure 2.13.

For successful maximum power point tracking, the controller changes the duty cycle of the converter so as to match the input impedance to the load impedance. The tracking and non-tracking regions of the buck converter in MPPT application are depicted in figure 2.14.

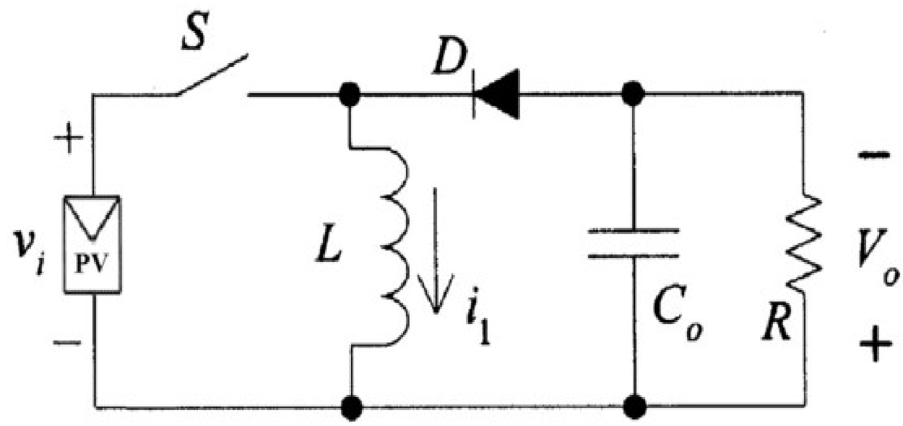

Figure 2.13 Inverting Buck-Boost converter circuit

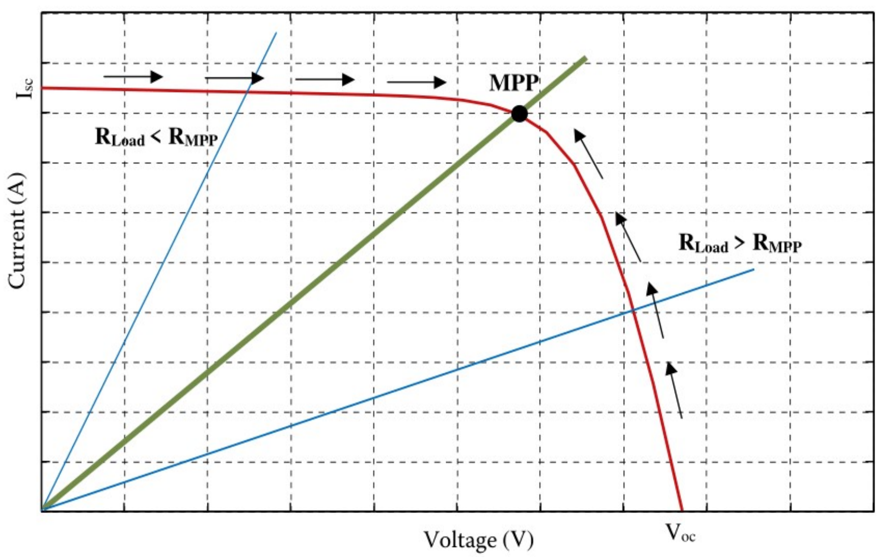

Figure 2.14 Buck-Boost converter MPP tracking region

Because of its known MPP tracking capacity, the buck-boost converter was considered for this study. An elaborate small signal analysis (Paja, 2012 of this converter is presented in chapter 3.

2.3 The Single-Phase Voltage Source Inverter

Many different inverter topologies have been developed over time. Based on their circuit configurations and input sources these inverters can be divided into half bridge

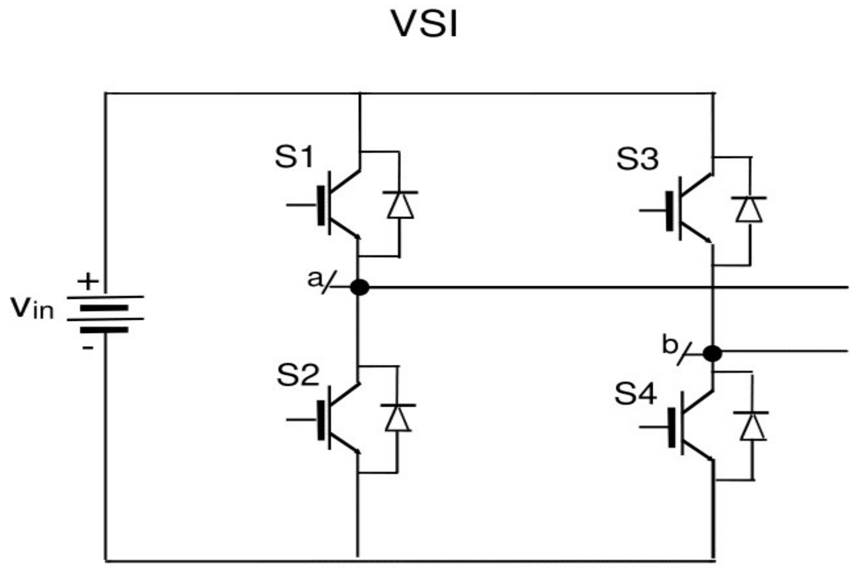

Figure 2.15 Single phase full bridge inverter

inverters, full bridge inverters, current source inverters or voltage source inverters. These devices can further be divided into buck, boost, buck boost inverters based on the change in voltage amplitude from input to output. In this thesis, a buck type full H bridge voltage source inverter (VSI was implemented. The structure of this type of inverter is shown in figure 2.15.

The single phase H bridge voltage source inverter is the fundamental block the second stage of the proposed system. Together with the closed-loop controller the VSI will allow for the regulation of voltage in the required range.

The most common technique used to in inverter technology is pulse width modulation. Although the output of the inverter when operated under pulse width modulation is a highly distorted, the total harmonic distortion is relatively lower to that of a square wave. This characteristic reduces the filter requirements thus reducing the total size of the design. Additionally, PWM in conjunction with a suitable control technique allows for the regulation of the amplitude of the inverter output voltage, which in the scope of this thesis is the primary function of the second stage of the system. The main drawback when it comes to PWM are switching losses. Two of the main types of PWM techniques are unipolar modulation and bipolar modulation.

Unipolar pulse width modulation test come with more complex control circuits and in many literature this technique has been found to be associated with high levels of common mode voltage when implemented in non-isolated grid connected PV systems.Although less efficient, the bipolar pulse width modulation technique presents some advantages such as constant common mode voltage and simple implemntation. In this study, the bipolar pulse width modulation technique was implemented.

The implementation of bipolar pulse width modulation in voltage source inverters is done by comparing a triangular waveform, known as the carrier waveform to a sinusoidal reference voltage signal, known as the control signal and passing the output through a logic that controls the diagonally opposite switches of the H bridge simultaneously, in this case the switch pairs S1, S4 and S2, S3. Typically, the frequency of the carrier waveform much greater than the frequency of the control signal (Hafezi, 2014).

2.3.1 Harmonic Mitigation

The switching operation of the pulse width modulation technique (PWM) in H bridge inverters generates voltage harmonics at the multiple values of the switching frequency. In order to attenuate these harmonics and produce the required sinusoidal waveform, a low-pass filter is required.

Figure 2.16 shows the general structures of three of the most commonly used types of filters, the L, the LC, the LCL filters. As suggested, the L filter consists of just an inductor, the LC type filter consists of an inductor and a capacitor. The LCL type filter consists of two inductors, one inductor on the inverter output side and the other on the load side, with the capacitor connected in parallel in between the inductances. These three types of filters differ a lot in terms of their ability to suppress the inverter output harmonics. The L filter has an attenuation of only -20 dB/dec , implying that a large sized inductor is required in order to get a fair amount of output harmonic reduction.

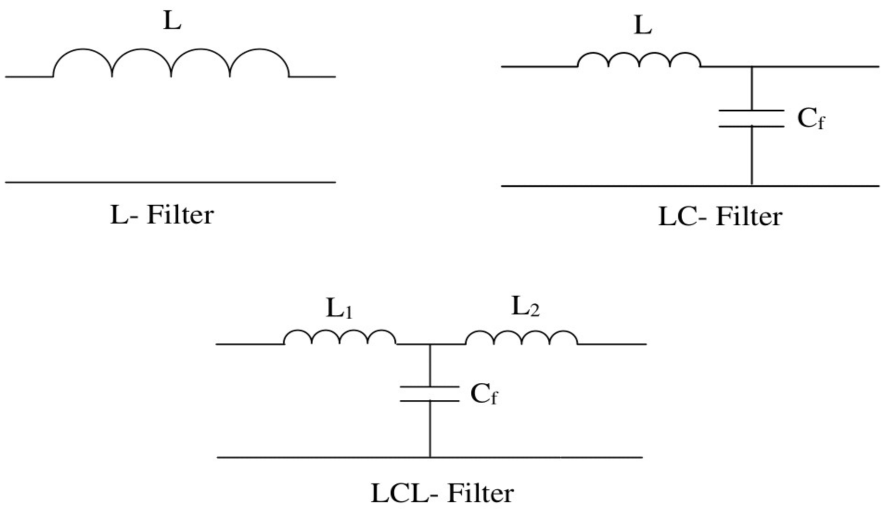

Figure 2.16 L filter, LC filter and LCL filter

The LC filter, on the other hand, can achieve an attenuation of -40 dB/dec and due to the presence of the capacitor the size of the inductor can be reduced, however, in grid tied systems the resonance frequency of the filter is dependent upon the grid impedance. The LC filter is fairly effective in standalone systems. The LCL filter, which has grown to be the industry standard in grid connected systems, when compared to the LC filter can provide decoupling between the grid impedance and the filter is significantly higher attenuation levels of up to -60 dB/dec frequencies above the resonance frequency. Other more advanced filters exist such as the LLCL filter, however, the design of these higher order filters becomes more complex. In this thesis, due to its high performance and relatively simpler design, the LCL filter was chosen for harmonic mitigation at the output of the inverter in the second stage of the system.

2.3.1.1 The LCL Filter

It is important to note that inherent resonant peak of the LCL filter causes instability in systems, as such, in order to stabilize the system, these types of filters are usually implemented in conjunction with a damping mechanism to improve the control of the system. There are generally two types of damping methods that are commonly used, namely passive damping and active damping. Passive damping is the simplest when it comes to design and implementation, however this method introduces additional power losses and in some cases reducing the performance of the LCL filter. Passive damping is done by adding a resistance in parallel to the LCL filter or in series with the filter capacitance (Kinas, 2018). The design of passive filter components requires accurate approximation of the ripple quantities present in different currents and voltages (Sahoo, 2014). Active damping on the other hand utilizes a well designed control technique and does not introduce any power losses . The design procedure for active damping for the system within LCL filter is complex but some researchers such as (Zhang, 2014) have developed systematic methods to address this.

The inverter side inductance is designed so as to reduce the current ripple at the output of the inverter, while the second inductance, commonly known as the grid side inductance for grid connected systems is related to the inverter side inductance by a ratio known as the inductance rate (r) which is dertermined through the relationship between the outer current ripple and enough current ripple (Yoon, 2010).

2.3.2 Voltage-Oriented Closed-Loop Control

Two of the most widely used controllers in voltage source inverters are the PID controller and the proportional resonant (PR) controller. The PI controller in its general form, i.e. in the stationary frame, is not preferable for the control of AC sources since it is incapable of eliminating the steady-state error. This type of controller is used in three-phase AC applications only when it is in the synchronous (dq) reference frame, whereby the three-phase AC quantities are transformed into DC quantities, however, for single phase systems there are additional computations which are required to facilitate this transformation, making the whole design procedure cumbersome.

One important design consideration when it comes to voltage source inverters is the switching frequency. The selection of the switching frequency for the pulse width modulation single phase inventors is usually a trade-off between reducing switching

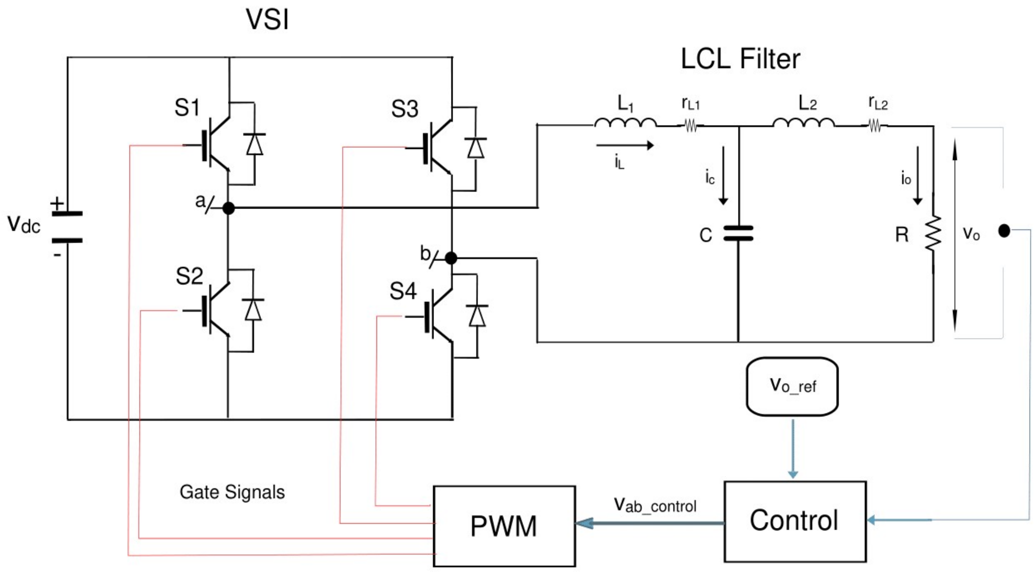

Figure 2.17 Voltage oriented closed loop control

losses and reducing the total harmonic distortion of the output waveform (THD), and in order to reduce switching power losses while successfully attenuating higher order harmonics, carefully choice and design of the output filter to the inverter is essential (Raja, 2016.

2.3.2.1 Proportional Resonant Control

The proportional resonant controller (PR) is a type of stationary frame controller that is capable of eliminating the steady-state error in AC systems by providing gains at a certain frequency, known as the resonant frequency. This controller is based on the internal model principal (IMP), according to which if the closed-loop system stability is guaranteed then the PR controller will ensure a zero steady-state error for sinusoidal reference tracking and disturbance rejection at the determined frequency. Additionally, because of the fact that the infinite gain of the PR controller is at the certain known frequency band, it allows for selective harmonic compensation (Narayana, 2018). The PR controller can be successfully implemented in grid connected or standalone solar PV inverter systems to control the output voltage. The operation of the PR controller is comparable to the PI controller when used to regulate

DC parameters, with the only difference being that integration in a PR controller happens only at frequencies in the proximity of the resonant frequency, thus avoiding the steady-state error (Teodorescu, 2004).

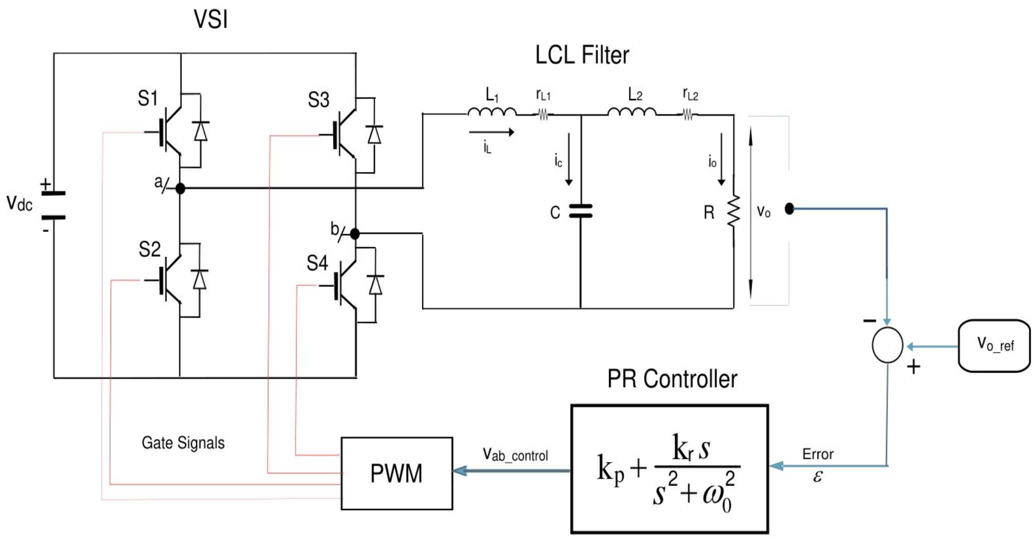

Figure 2.18 Proportional Resonant closed loop voltage control

2.3.2.2 PID Control

The PID controller is a combination of three types of controllers, the Proportional controller (k_p), the Integral controller (k_i) and the Derivative controller (k_d). These three parameters combined together such a way that the overall controller is capable of stabilizing the system. This proportional control on its own is not capable of eliminating the steady-state error but decreases the rise time. The integral controller is capable of decreasing the steady-state error but increases the overall settling time of the system. The derivative parameter k_d, is capable of reducing the overshoot and the settling time (Aström, 2002).

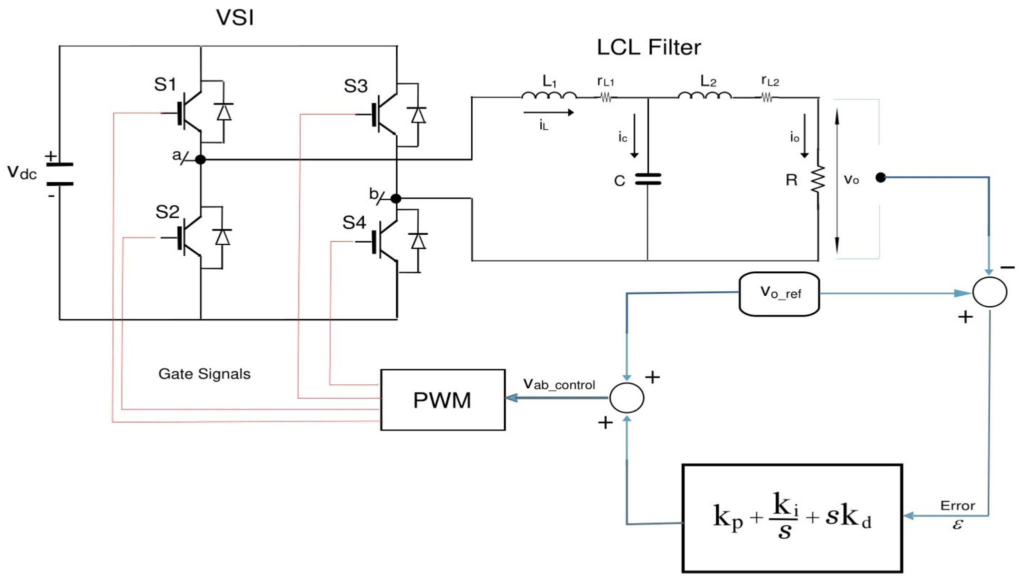

Figure 2.19 PID closed loop voltage control

2.4 The Brushless DC Motor Drive

In general, BLDC motors are synchronous motors i.e. the magnetic field induced by the stator rotates at the same frequency as the magnetic field that the rotor generates. In terms of construction the brushless DC motor (BLDC has similarities to three-phase AC motors and brushed direct current motors. The stator of this machine is made up of layers of laminated steel, with windings placed in between the slots. Typically, the coils and the stator are wound in such a way that the motor produces a trapezoidal back electromagnetic force (EMF. The BLDC motor is also commonly referred to as the electronically commuted motor since it does not have any brushes, and at certain positions of the rotor commutation is done electronically in a six – step manner using a sensory circuit, usually with Hall effect sensors. Sensorless control techniques of BLDC motors have also been discussed in literature. The speed of the BLDC motor is directly proportional to the voltage applied across the stator.

For transient analysis, the BLDC motor can be modeled as follows:

$$v = Ri + L_s \frac{d}{dt} i + e \tag{2.1}$$

$$\begin{bmatrix} V_a \\ V_b \\ V_c \end{bmatrix} = \begin{bmatrix} R & 0 & 0 \\ 0 & R & 0 \\ 0 & 0 & R \end{bmatrix} \begin{bmatrix} i_a \\ i_b \\ i_c \end{bmatrix} + \begin{bmatrix} L_s & 0 & 0 \\ 0 & L_s & 0 \\ 0 & 0 & L_s \end{bmatrix} \frac{d}{dt} \begin{bmatrix} i_a \\ i_b \\ i_c \end{bmatrix} + \begin{bmatrix} e_{as} \\ e_{bs} \\ e_{cs} \end{bmatrix} \quad (2.2)$$

Where i_a , i_b , i_c are phase currents and V_a, V_b , V_c are phase voltages, L_s is the self-inductance, R is the winding resistance. e_{as}, e_{bs} and e_{cs} are the induced voltages. These voltages are time varying and speed dependent.

The electromagnetic torque can be expressed as

$$T_e = \frac{1}{\omega_r} \left(e_{as} i_a + e_{bs} i_b + e_{cs} i_c \right) \quad (2.3)$$

Interaction of the electromagnetic torque with the load torque is described by the equation:

$$T_e = T_L + J \frac{d\omega_r}{dt} + B\omega_r \quad (2.4)$$

Where T_L is the load torque, J is the inertia of the motor, B is viscous damping, ω_r is the rotor speed.

These differential equations can be solved simultaneously under the phase voltage is generated from the three-phase inverter. In the scope of this study, three-phase inverter of the BLDC drive is fed from the output of a single phase bridge rectifier which is fed by the two-stage PV system described in this thesis.

CHAPTER THREE
SYSTEM DESIGN AND ANALYSIS

3.1 System Sizing

The sizing of the PV generator depends mainly on the current and voltage levels at which the system is expected to operate. The solar modules are connected either in series or in parallel or both in order to provide the required power, voltage, current ratings. Series connection of PV modules results in an overall higher voltage output at the terminals of the PV array. Such a connection is shown in figure 3.1. Parallel connection of the PV modules results in an overall higher current output. Such a connection is shown in figure 3.2. In order to correctly size the system, it is necessary to have information about the PV module itself, the conditions under which the system is expected to operate in the load. The PV systems that operate in combination with a battery, it is allowable to have an undersized PV array since the load is fed from the terminals of the battery and not directly from the PV. However, in the case of the system proposed in this thesis, there is no battery as an intermediate component between the DC-DC converter and the inverter. As such, the sizing of the system is of paramount importance.

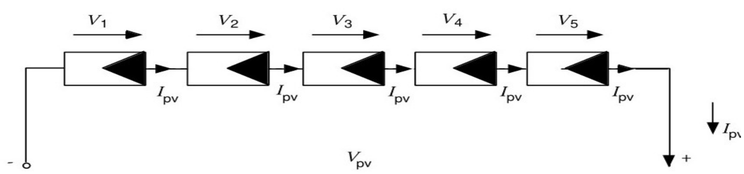

Figure 3.1 PV modules series connection

The system designed in this thesis has specifications such that it is expected to operate continuously at irradiation levels of $1{,}000 W/m^2$ and $600 W/m^2$ which correspond to the global average irradiation level on a typical summer day and on a typical winter day respectively. The system is expected to supply 240 VAC at the output of the inverter to a load rated 3 kW. Since the system is going to be implementing a maximum power point tracking algorithm, it is necessary to use the

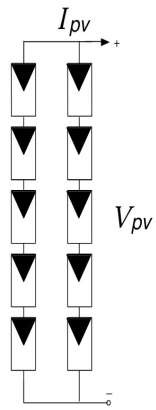

Figure 3.2 Parallel connection of strings of PV modules

data sheets from the manufacturer to establish the maximum power and voltage that the module is capable of supplying under the worst conditions i.e. $600W/m^2$. It is important to note that when MPPT techniques are used, a trade-off happens between extracting the maximum power from the PV array and being able to control the output voltage of the DC to DC converter. The PV array used in this thesis has two parallel strings of 14 series connected solar modules, type 1Soltech 15TH-215-P. The characteristics of this PV array irradiance levels $1{,}000W/m^2$ and $600W/m^2$ as well as temperature variations of 25°C, 40°C, 15°C are shown in figure 4.2 and figure 4.3.

3.2 Buck-Boost Converter Stability Under Varying Duty Cycle

For this thesis, the buck boost DC-DC converter was chosen for application in the first stage of the system because of its ability to track the maximum power point of the PV array in two regions as highlighted in chapter 2. In this section, analysis of the behavior of this DC-DC converter in the case of rapid change in duty cycle is carried out to assess the expected performance and stability when operating under a direct duty cycle perturbation P&O MPPT algorithm. This investigation utilizes the state-space averaged small signal modelling method to derive the transfer functions of the parameters of interest, which are then analyzed to determined the expected behaviour of the system.

3.2.1 Small Signal State-Space Modeling of Buck-Boost Converter

The state-space modeling of all DC-DC converters is based on two operational states: the ON state, over time dT and the OFF state, over time (1-d)T , where T is the period of steady state operation and d is the duty cycle.The method of developing the state space model is presented in this section. The complete MatLab code for the state-space modeling of the Buck-Boost converter is provided in appendix A.1 .

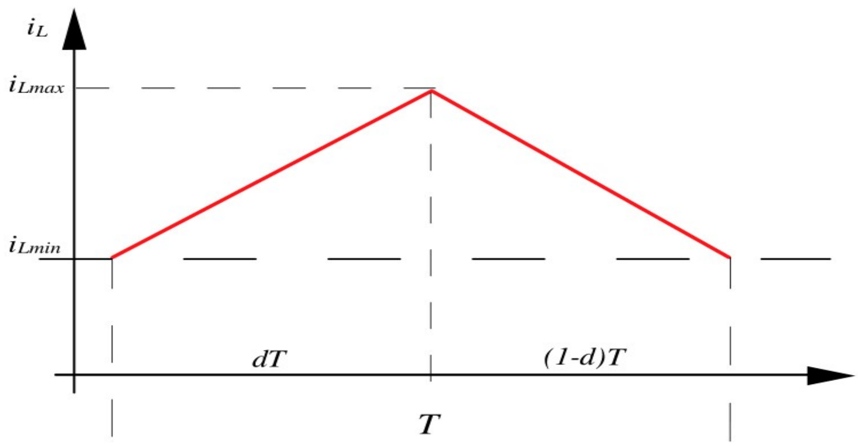

Figure 3.3 Inductance current

Figure 3.3 illustrates the variation in inductor current in the ON and OFF states for continuous conduction mode operation (CCM

A representation of the ON and OFF states of the buck-boost converter including all system parameters is shown in figure 3.4 , where V_{in} is the input voltage, V_c is the capacitor voltage, L is the inductance value, r_L is the resistance of the inductor, r_C is the capacitor resistance, V_d is the voltage drop across the diode, V_j is the voltage drop across the switch in the on state, r_j is the resistance of the switch, r_d is the resistance of the diode, i_o is the load current, R_o is the load resistance, d is the duty cycle, V_o is the output voltage.

The ON state: In this mode the switch is closed.

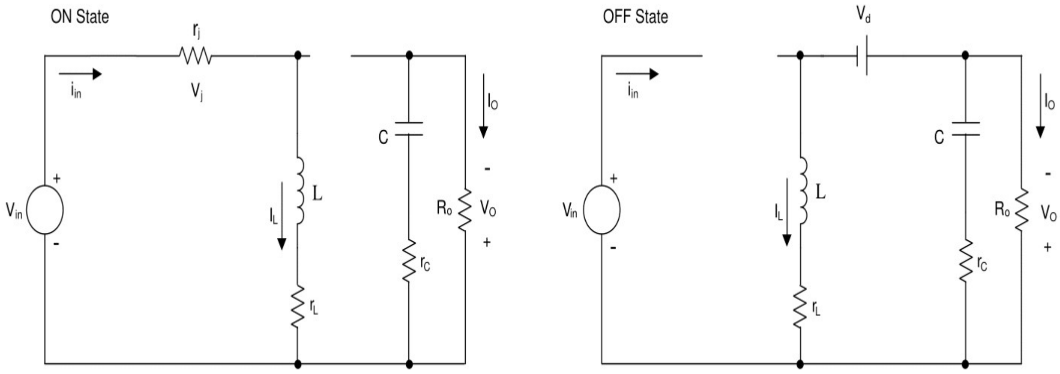

Figure 3.4 Buck-Boost Converter in ON and OFF states

This operational mode can be represented in the state-space form as:

$$\dot{x} = A_1 x + B_1 u \tag{3.1}$$

$$y = C_1 x + D_1 u \tag{3.2}$$

Where,

$$x = \begin{bmatrix} i_L \\ V_c \end{bmatrix} u = \begin{bmatrix} V_{in} \\ i_o \\ V_j \\ V_d \end{bmatrix} y = \begin{bmatrix} V_o \\ i_o \\ i_L \end{bmatrix}$$

$$A_1 \ = \begin{bmatrix} -\left(\frac{r_L + r_j}{L}\right) & 0 \\ 0 & \left(\frac{-1}{R_o + r_C}\right) \end{bmatrix} \tag{3.3}$$

$$B_1 \ = \begin{bmatrix} \frac{1}{L} & 0 & \frac{-1}{L} & 0 \\ 0 & \frac{-R_o}{(R_o + r_C)C} & 0 & 0 \end{bmatrix} \tag{3.4}$$

$$C_1 \ = \begin{bmatrix} 0 & \frac{R_o}{R_o + r_C} \\ 0 & \frac{1}{R_o + r_C} \\ 1 & 0 \end{bmatrix} \tag{3.5}$$

$$D_1 = \begin{bmatrix} 0 & \frac{-R_o r_C}{(R_o+r_C)} & 0 & 0 \\ 0 & \frac{R_o}{(R_o+r_C)} & 0 & 0 \\ 0 & 0 & 0 & 0 \end{bmatrix} \tag{3.6}$$

The OFF state: In this mode the switch is open.

This operational mode can be represented in the state-space form as:

$$\dot{x} = A_2 x + B_2 u \tag{3.7}$$

$$y = C_2 x + D_2 u \tag{3.8}$$

Where,

$$x = \begin{bmatrix} i_L \\ V_c \end{bmatrix} u = \begin{bmatrix} V_{in} \\ i_o \\ V_j \\ V_d \end{bmatrix} y = \begin{bmatrix} V_o \\ i_o \\ i_L \end{bmatrix}$$

$$A_2 = \begin{bmatrix} -\left(\frac{R_o r_L + R_o r_C + r_C r_L + R_o r_d + r_C r_d}{L(R_o+r_C)}\right) & \frac{-R_o}{(R_o+r_C)L} \\ \frac{R_o}{(R_o+r_C)C} & \frac{-1}{(R_o+r_C)C} \end{bmatrix} \tag{3.9}$$

$$B_2 = \begin{bmatrix} 0 & \frac{R_o r_C}{(R_o+r_C)L} & 0 & \frac{-1}{L} \\ 0 & \frac{-R_o}{(R_o+r_C)C} & 0 & 0 \end{bmatrix} \tag{3.10}$$

$$C_2 = \begin{bmatrix} \frac{R_o r_C}{R_o+r_C} & \frac{R_o}{R_o+r_C} \\ \frac{r_C}{R_o+r_C} & \frac{1}{R_o+r_C} \\ 1 & 0 \end{bmatrix} \tag{3.11}$$

$$D_2 = \begin{bmatrix} 0 & \frac{-R_o r_C}{(R_o+r_C)} & 0 & 0 \\ 0 & \frac{R_o}{(R_o+r_C)} & 0 & 0 \\ 0 & 0 & 0 & 0 \end{bmatrix} \tag{3.12}$$

By combining the expressions from the ON state and OFF state, we end up with a single set of state-space equations representing the entire operation of the converter as follows:

$$\dot{x} = A_k x + B_k u \tag{3.13}$$

$$y = C_k x + D_k u \tag{3.14}$$

Where,

$$A_k = A_1 d + A_2 (1-d) = A_1 d + A_2 d'$$

$$B_k = B_1 d + B_2 (1-d) = B_1 d + B_2 d'$$

$$C_k = C_1 d + C_2 (1-d) = C_1 d + C_2 d'$$

$$D_k = D_1 d + D_2 (1-d) = D_1 d + D_2 d'$$

By substituting the initial equations into these expressions, the coefficients A$_k$, B$_k$, C$_k$, and D$_k$ take the form:

$$A_k = \begin{bmatrix} \frac{-(R_o+r_C)(r_j+r_L)+(r_j-r_d)(R_o+r_C)d'-R_o r_C d'}{(R_o+r_C)L} & \frac{-R_o d'}{(R_o+r_C)L} \\ \frac{R_o d'}{(R_o+r_C)C} & \frac{-1}{(R_o+r_C)C} \end{bmatrix} \tag{3.15}$$

$$B_k = \begin{bmatrix} \frac{1-d'}{L} & \frac{d' R_o r_C}{(R_o+r_C)L} & \frac{d'-1}{L} & \frac{-d'}{L} \\ 0 & \frac{-R_o}{(R_o+r_C)C} & 0 & 0 \end{bmatrix} \tag{3.16}$$

$$C_k = \begin{bmatrix} \frac{d' R_o r_C}{R_o+r_C} & \frac{R_o}{R_o+r_C} \\ \frac{d' r_C}{R_o+r_C} & \frac{1}{R_o+r_C} \\ 1 & 0 \end{bmatrix} \tag{3.17}$$

$$D_k = \begin{bmatrix} 0 & \frac{-R_o r_C}{(R_o+r_C)} & 0 & 0 \\ 0 & \frac{R_o}{(R_o+r_C)} & 0 & 0 \\ 0 & 0 & 0 & 0 \end{bmatrix} \tag{3.18}$$

In the case of a non-varying duty cycle, the combined state equations can be assumed to be linear, however, in reality, in order to regulate the voltage in accordance with the reference, the duty cycle is constanly changing, hence from that perspective, the set of equations representing the DC-DC converter is non-linear and needs to be linearized around an operating point where the duty cycle is nominal. For the linearization of the state equations and formulation of the averaged small signal transfer functions of the buck-boost converter, a Matlab code developed (see appendix A1.). The following tranfer functions were extracted:

1. The transfer function of output voltage to duty cycle
2. The transfer function of inductor current to duty cycle

Analysis was done in the MatLab environment.

3.2.2 Analysis of Findings

In order to analyse the stability and performance of the buck-boost converter when subjected to rapid changes of direct duty cyle , averaged small-signal transfer functions of the inductor current and output voltage with respect to duty cycle were developed and their step responses and pole-zero maps were studied.

The output voltage to duty cycle small-signal transfer function of a Buck-Boost converter generated using the Matlab code presented in appendix A1 is a continuous-time transfer function of the form:

$$\boldsymbol{G}(\boldsymbol{s}) = \frac{-1.065e20s^2 - 1.065e27s + 3.272e30}{6.587e21s^2 + 5.447e23s + 1.655e27}$$

In order to analyze the stability of the system and expected response for this parameter pairing, the pole zero map and step response were obtained. Figure 3.5 shows the step response of the small signal transfer function of the output voltage with respect to the duty cycle of a Buck-Boost converter. Figure 3.6 Shows the pole zero map of the small signal transfer function of the output voltage with respect to the duty cycle of a Buck-Boost Converter.

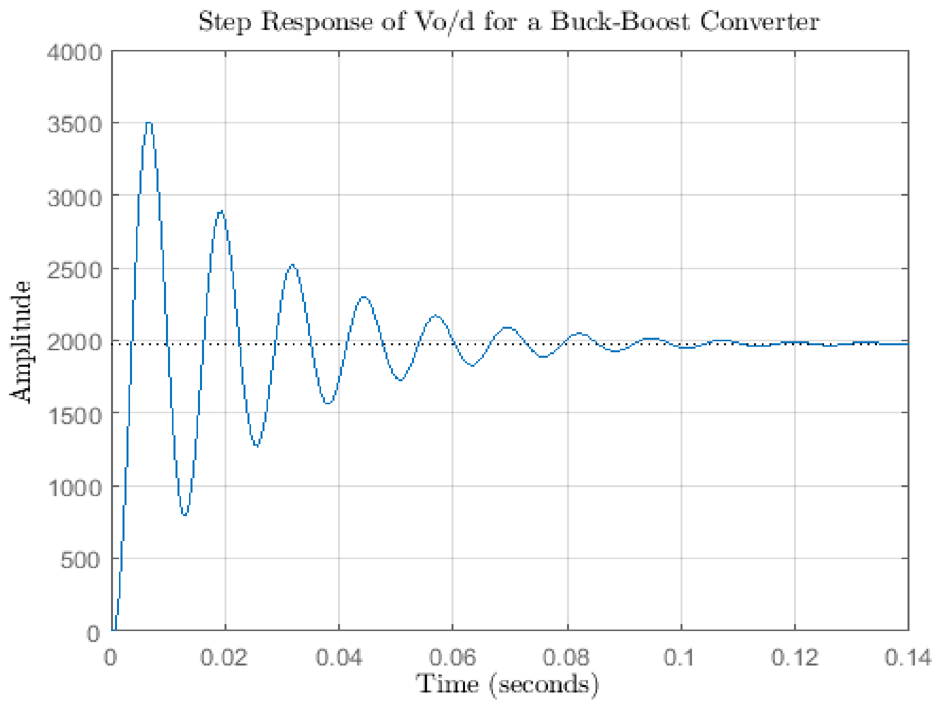

Figure 3.5 Step response of output voltage with respect to duty cycle for Buck-Boost converter

The output voltage to duty cycle transfer function of a Buck-Boost converter is a second order transfer function whose pole zero map and step response have been represented in figure 3.5 and figure 3.6. As seen in the pole zero map , the transfer function has a one pair of complex conjugate poles that lie in the left half of the S – plane at points S = -41.3 + 500i and S =-41.3 - 500i. The transfer function also has two zeros, one located in the left-handside of the S plane at point , located at point S = -1e7.and the other located on the right hand side of the S plane at point S = 3.07e3. In terms of stability, it can be said that since all the poles of the transfer function are seen to be on the left-hand side of the S plane, the output voltage of this converter is expected to be stable under rapid variations in the duty cycle by the action of the

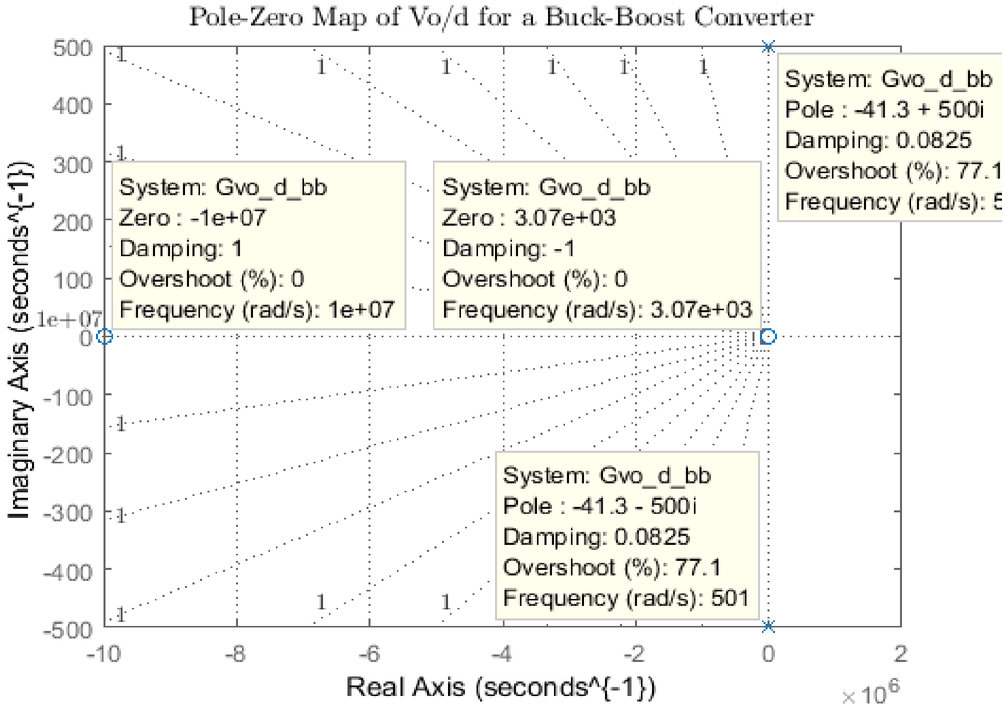

Figure 3.6 Pole-Zero map of output voltage with respect to duty cycle for Buck-Boost converter

direct duty-cycle perturbation MPPT algorithm. However, due to the complex conjugate nature of these poles, an oscillatory component is induced into the system. Since the poles are away from the imaginary axis, the oscillations are expected to decay exponentially towards the steady state operating point. The step response of the transfer function of output voltage to duty cycle, illustrated in figure shows that the settling time of the response is about 0.095 seconds, with a rise time of 0.0021 seconds. The observed percentage overshoot is 77.3%. Table 3.1 shows the step response characteristics of this transfer function.

The inductor current to duty cycle small-signal transfer function of a Buck Boost converter generated using the Matlab code presented in appendix A1 is a continuous-time transfer function of the form:

$$\boldsymbol{G}(\boldsymbol{s}) = \frac{3.293e27s + 4.721e29}{3.293e22s^2 + 2.724e24s + 8.275e27}$$

Table 3.1 Step response characteristics of output voltage to duty cycle of a Buck-Boost converter

Parameter	Value
Rise Time	0.0021
Settling Time	0.0950
Settling min.	796.8459
Settling max.	3.5050e+03
Overshoot	77.3037
Undershoot	0.1019
Peak	3.5050e+03
Peak Time	0.0069

In order to analyze the stability of the system and expected response for this parameter pairing, the pole zero map and step response were obtained. Figure 3.7 shows the step response of the small signal transfer function of the inductor current with respect to the duty cycle of a Buck-Boost converter. Figure 3.8 shows the pole zero map of the small signal transfer function of the inductor current with respect to the duty cycle of a Buck-Boost converter.

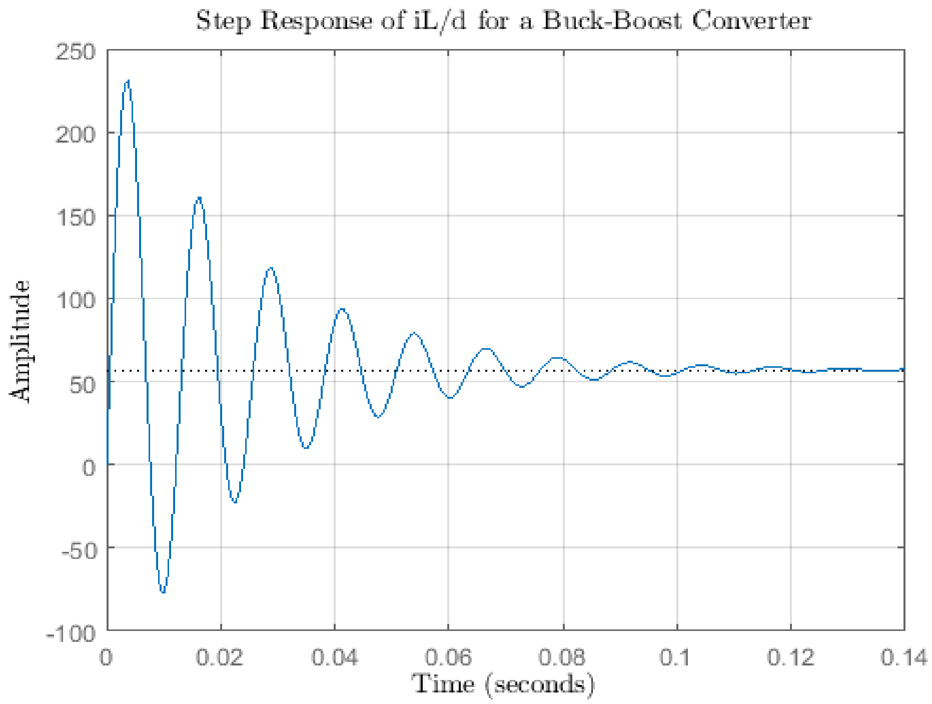

Figure 3.7 Step response of the inductor current with respect to duty cycle for Buck-Boost converter

The inductor current to duty cycle transfer function of a Buck-Boost converter is a second order transfer function whose pole zero map and step response have been

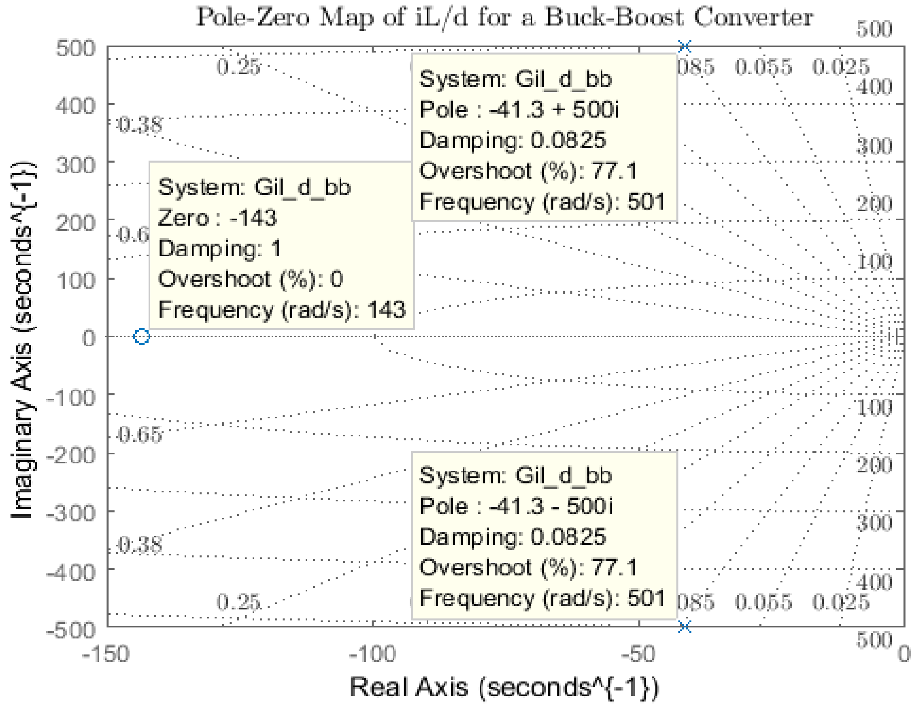

Figure 3.8 Pole-Zero map of inductor current with respect to duty cycle for Buck-Boost converter

represented in figure 3.7 and figure 3.8. As seen in the pole zero map , the transfer function has a one pair of complex conjugate poles that lie in the left half of the S – plane at points S = -41.3 + 500i and S =-41.3 - 500i. The transfer function also has a zero in the left-handside of the S plane, located at point S = -143. In terms of stability, it can be said that since all the poles of the transfer function are seen to be on the left-hand side of the S plane, the inductor current of this converter is expected to be stable under rapid variations in the duty cycle by the action of the direct duty-cycle perturbation MPPT algorithm. However, due to the complex conjugate nature of these poles, an oscillatory component is induced into the system. Since the poles are away from the imaginary axis, the oscillations are expected to decay exponentially towards the steady state operating point. The step response of the transfer function of inductor current to duty cycle, illustrated in figure shows that the settling time of the response is 0.0981 seconds, with a rise time of 4.5533e-04 seconds. The observed percentage overshoot is 305.4%. Table 3.2 shows the step response characteristics of this transfer function.

Table 3.2 Step response characteristics of inductor current to duty cycle of a Buck-Boost converter

Parameter	Value
Rise Time	4.5533e-04
Settling Time	0.0981
Settling min.	-77.4341
Settling max.	231.2790
Overshoot	305.4159
Undershoot	135.7365
Peak	231.2790
Peak Time	0.0038

From the results obtained in this investigative study, it is expected that the buck-boost converter because of its stability and fast response exhibits satisfactory performance charactirictics when used in conjuction with the direct duty cycle perturbation maximum power point tracking algorithm.

3.3 Closed-Loop Voltage Control of Single Phase LCL-Filtered VSI

This section presents the method used in this thesis to develop the plant model used in the evaluation of the control parameters/gains of the PID and PR controllers described in chapter 2.

3.3.1 Mathematical Modeling of Averaged VSI-LCL System

In order to derive the control loop for the VSI-LCL model so as to regulate the output voltage, v_o it is necessary to determine the average value dynamic model of the system (Guerrero, 2005). Defining the parameters of the system, we have:

$$\langle v_{ab} \rangle = v_{dc} S \tag{3.19}$$

where, $S -$ represents the switching function of the bipolar modulation scheme, depending on the states of switches S1, S2, S3 and S4.

$\langle v_{ab} \rangle -$ is the average value of the voltage at the output of the inverter.

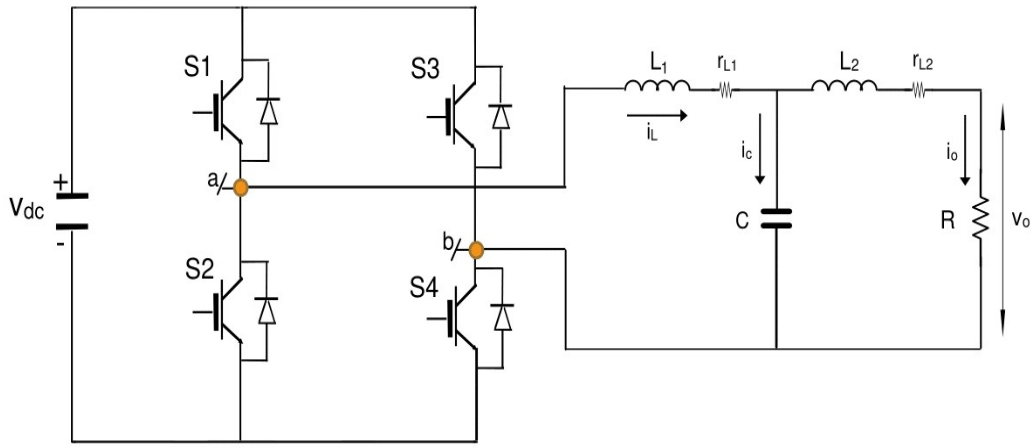

Figure 3.9 VSI-LCL System

$v_{dc} -$ is the DC voltage at the input of the inverter.

$$i_c = i_L - i_o = C\frac{dv_o}{dt} \tag{3.20}$$

where, $i_c -$ represents the capacitor current, $i_L -$ represents the current at the output of the inverter, i_o- represents the load current, v_o- represents the output voltage as seen on the load side.

$$v_c = \frac{1}{C}\int i_c = i_o\,(R + r_{L_2}) + L_2\frac{di_o}{dt} \tag{3.21}$$

where, L_2 $-$ is the LCL filter output inductance , R $-$ represents the load, r_2- represents the resistance of the inductance L_2.

$$\langle v_{ab}\rangle = \frac{1}{C}\int i_c + L_1\frac{di_L}{dt} + i_L\,r_{L_1} \tag{3.22}$$

Where, L_1 is the LCL filter output inductance, C represents the LCL filter capacitor, r_1 represents the resistance of the inductance L_1.

By combining equations (3.21) and (3.22), we have the following expression:

$$\langle v_{ab}\rangle = i_o\,(R + r_{L_2}) + L_2\frac{di_o}{dt} + L_1\frac{di_L}{dt} + i_L\,r_{L_1} \tag{3.23}$$

$$i_c = C\frac{dv_o}{dt} \tag{3.24}$$

$$i_o = \frac{v_o}{R} \;\;,\;\; R \gg r_{L_2} \tag{3.25}$$

By substituting equations (3.24) and (3.25) into (3.23), we get an expression that describes the open-loop averaged output dynamics of the VSI-LCL model, equation (3.27).

$$\langle v_{ab}\rangle = \frac{v_o}{R}\left(R + r_{L_2}\right) + \frac{L_2}{R}\frac{dv_o}{dt} + CL_1\frac{d^2v_o}{dt^2} + \frac{L_1}{R}\frac{dv_o}{dt} + \frac{v_o}{R}\,r_{L_1} \tag{3.26}$$

$$\langle v_{ab}\rangle = CL_1\frac{d^2v_o}{dt^2} + (\frac{L_2 + L_1}{R} + r_{L_1}C)\frac{dv_o}{dt} + v_o\left(1 + \frac{r_{L_1} + r_{L_2}}{R}\right) \tag{3.27}$$

Plant Model:

By taking equation (3.27) into the Laplace domain, we get:

$$\langle v_{ab}\rangle(s) = s^2v_o(s)\,CL_1 + sv_o(s)\left(\frac{L_2 + L_1}{R} + r_{L_1}C\right) + v_o(s)\left(1 + \frac{r_{L_1} + r_{L_2}}{R}\right)$$

Let, $\langle v_{ab}\rangle(s) = v_{ab}(s)$

$$v_{ab}(s) = v_o(s)\left[\frac{s^2(RCL_1) + s\left(L_2 + L_1 + Rr_{L_1}C\right) + \left(R + r_{L_1} + r_{L_2}\right)}{R}\right] \tag{3.28}$$

The transfer function for our plant model is expressed as:

$$\boldsymbol{G}(\boldsymbol{s}) = \frac{v_o(s)}{v_{ab}(s)} = \left[\frac{R}{s^2(RCL_1) + s\left(L_2 + L_1 + Rr_{L_1}C\right) + \left(R + r_{L_1} + r_{L_2}\right)}\right]$$

The plant model was used to determine the parameters of the controllers.

Proposed PID controller:

$$v_{ab\_control} = v_{o\_ref} + k_p\left(v_{o\_ref} - v_o\right) + k_i\int\left(v_{o\_ref} - v_o\right) + k_d\frac{d\left(v_{o\_ref} - v_o\right)}{dt} \tag{3.29}$$

PR controller:

$$v_{ab\_control} = k_p \left(v_{o\_ref} - v_o\right) + k_r \frac{s \left(v_{o\_ref} - v_o\right)}{s^2 + w_o^2} \tag{3.30}$$

In chapter 4, the simulation results of the proposed system using the methods discussed in previous chapters are presented and analyzed.

CHAPTER FOUR
SIMULATION RESULTS

This section presents the results from the simulation of the proposed two-stage system in the Matlab-Simulink environment. Simulation of the proposed system was done in a stage by stage manner. The goal was to first assess the performance of the DC power stage in isolation and to gain information necessary for the design of the second stage. In the second step, the DC and AC power stages were then simulated in conjunction and lastly, the complete PV pumping system with a BLDC motor was simulated.

In the simulation of the DC power stage, emphasis was put on observing the efficiency of the Buck-Boost converter in tracking the maximum power of the PV array under rapidly changing environmental conditions. For this experiment, variations in irradiance and temperature were based on realistic seasonal averages, whereby irradiance is at a high of $1{,}000 W/m^2$ on a typical summer day and at a low of $600 W/m^2$ on a typical winter day. The simulation of the DC stage was also aimed at investigating the performance of the PV array with varying ambient temparature. The reference signals are shown in Figure 4.1.

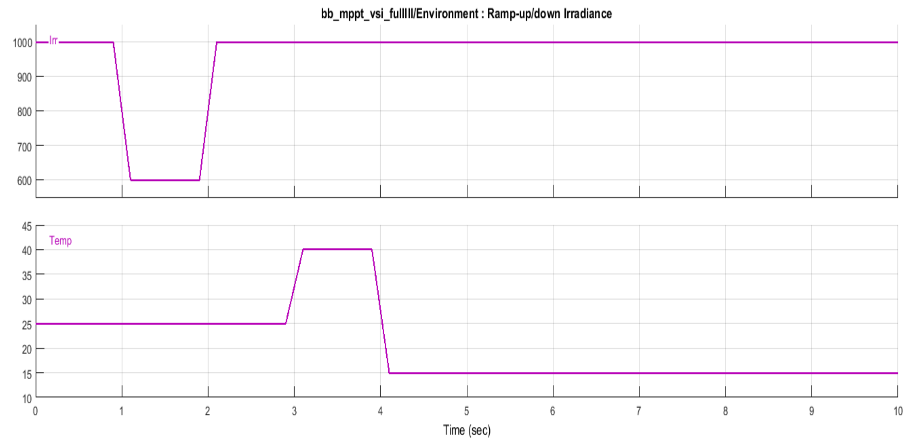

Figure 4.1 Variation of irradiance and temperation over the simulation period

4.1 Simulation of Isolated DC Power Stage

In order to analyze the DC stage of the proposed system as well as the performance of the MPPT algorithm in dynamically changing atmospheric conditions, the PV array in conjunction with the DC to DC buck-boost converter were simulated in isolation. In the first setup, the system was made to operate under a constant duty cycle of 0.5. In the second setup, the system was simulated with the duty cycle of the system being controlled by an MPPT perturb and observe algorithm. The environmental changes in irradiance and temperature were modeled using a Matlab signal block for irradiances of $1{,}000W/m^2$ and $600W/m^2$, and temperature variations of 25°C, 40°C and 15°C.

To understand the expected maximum power, create an MPP reference and determine the efficiency of the system at each of these levels of irradiance and temperature, the P – V characteristic curves of the chosen and configured 1Soltech 15TH-215-P array of modules as provided by the manufacturer were extracted and analyzed. Figure 4.3 shows the variation of the PV array voltage and power with changes in temperature. Figure 4.2 shows the variation of the PV array voltage and power with changes in irradiation.

The variations were as follows: At the time t = 0 seconds, the irradiance is $1{,}000W/m^2$ (rated value) and the temperature is 25°C (rated value). The expected maximum power under these conditions is 6,000W. From time t = 0.9 seconds to t = 1.1 seconds the irradiation drops from $1{,}000W/m^2$ to $600W/m^2$ while temperature is kept constant. From time t = 1.1 seconds to t = 1.9 seconds the environmental conditions are maintained and the expected maximum power is 3,600W. From time t = 1.1 seconds to t = 2.1 seconds the irradiance level is brought back up to $1{,}000W/m^2$ and the temperature remains the same. At t = 2.9 seconds the temperature is increased from 25°C to 40°C, where it is maintained from time t = 3.1 seconds up to time t = 3.9 seconds. In this period the irradiance is maintained at $1{,}000W/m^2$. The expected maximum power at this point is 5,600W. From time t = 3.9 seconds to time t = 4.1 seconds the temperature is dropped from 40°C to 15°C, with the irradiation being

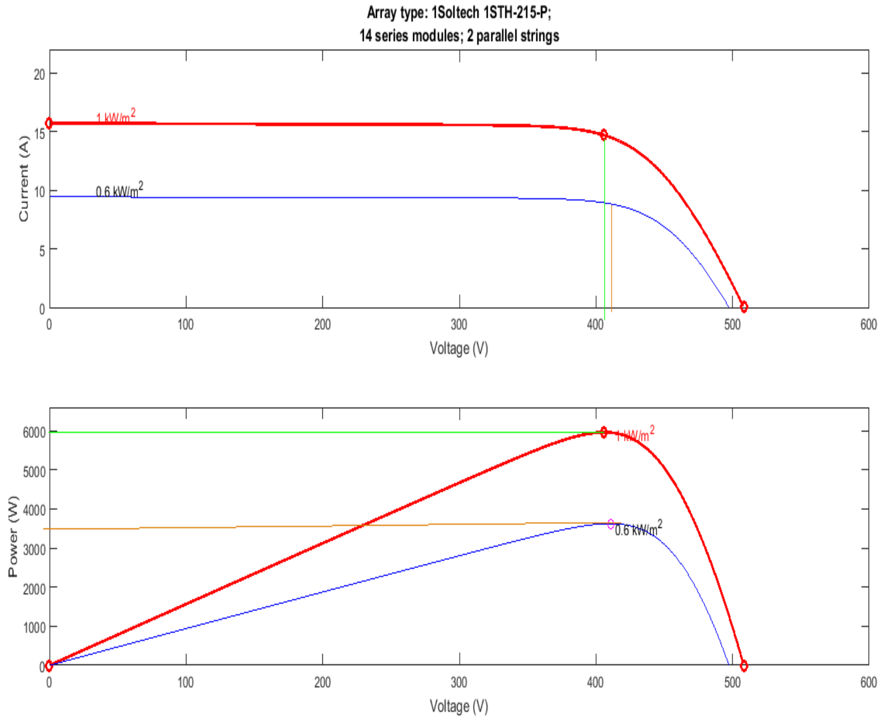

Figure 4.2 P-V characteristic of 1Soltech 15TH-215-P array undervarying irradiation

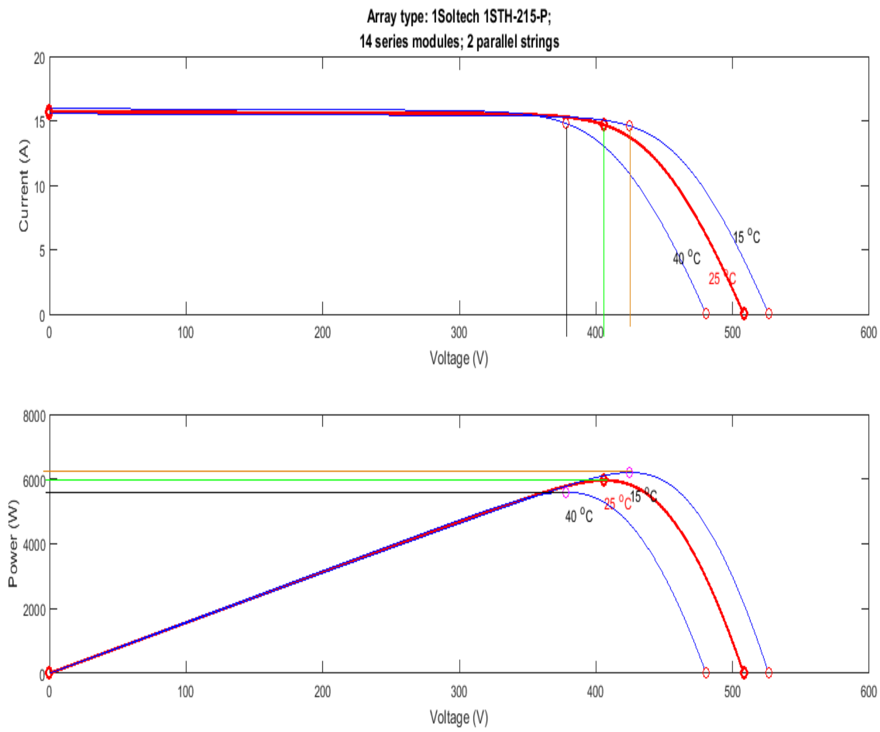

Figure 4.3 P-V characteristic of 1Soltech 15TH-215-P array undervarying temperature

kept at $1{,}000W/m^2$. Under these conditions, the expected maximum power of the PV array is 6,200W. At the 5s mark the simulation is stopped.

4.1.1 Simulation Under Constant Duty Cycle Operation

The simulation model setup for this stage is presented in appendix A.2.

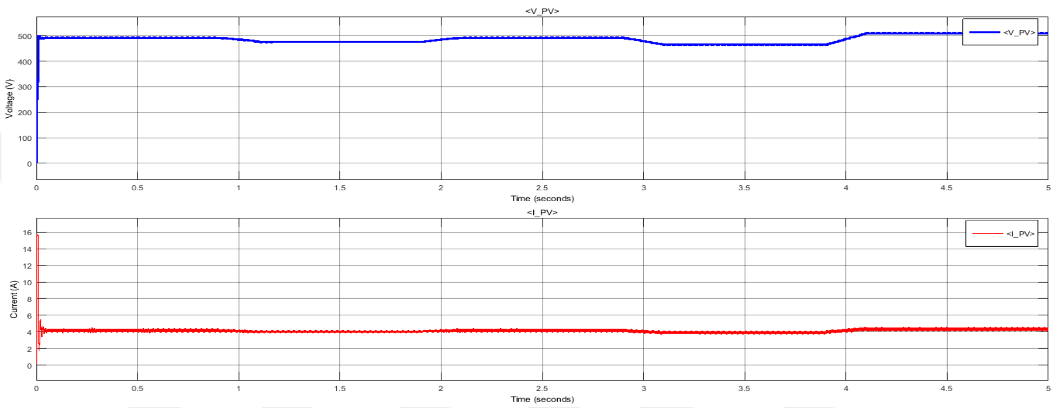

Figure 4.4 PV voltage and current under constant duty cycle operation

Figure 4.4 shows the PV output voltage and current when the DC stage is operated under constant duty cycle. The values of these parameters at the optimal conditions of irradiance and temperature are seen to be 490V and 4.2A. As the environmental conditions change according to the reference signal, the values of voltage and current are seen to drop when irradiance decreases and vice versa. When the temperature increases up to 40°C, the PV voltage and current are also seen to decrease, confirming the properties of the PV cell as described in chapter 2. However, when the temperature falls to 15°C, the values of voltage and current are seen to increase suggesting that the PV module selected in this study operates more efficiently at temperatures lower than the rated value.

Figure 4.5 shows a comparison of power values for the isolated DC system operating under constant duty cycle. The red plot (top) corresponds to the reference signal of the maximum power point of the PV system. The green plot (middle) shows the power that is available at the terminals of the PV array. The blue plot (bottom) shows the

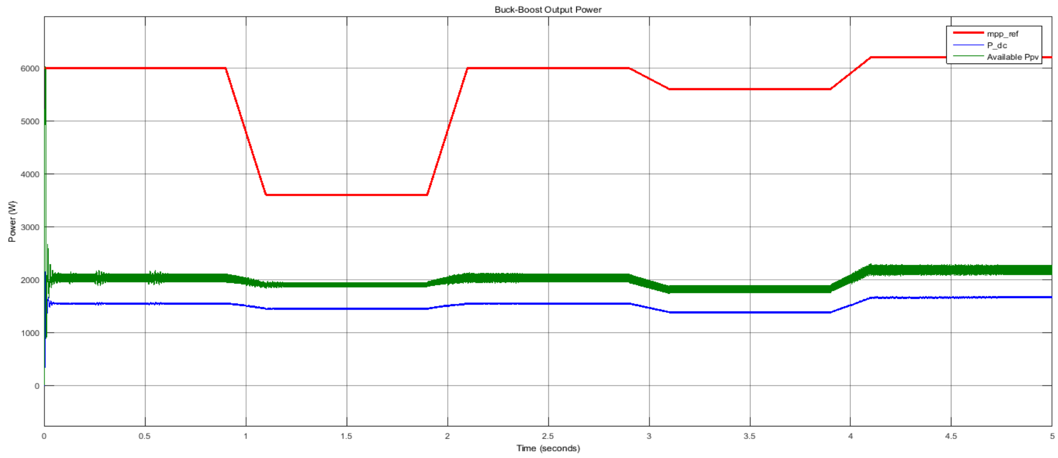

Figure 4.5 DC stage input-output power under constant duty cycle operation

power that is available at the output of the buck boost converter. It rated irradiance and temperature the maximum PowerPoint is at 6 kW, however there available power at the terminals of the PV array under these conditions is seen to be only around 2kW. The power available at the output of the buck boost converter, on the other hand is seen to be just around 1.75 kW. This shows that constant duty cycle operation of the DC stage is highly inefficient in terms of power extraction from the PV array.

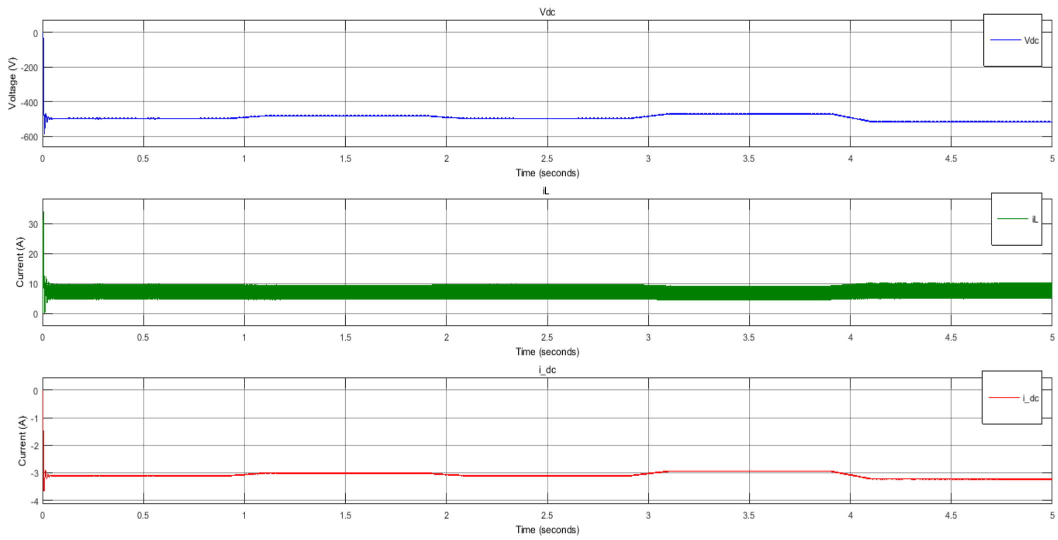

Figure 4.6 Buck-Boost output voltage, inductor current and output current under constant duty cycle

Figure 4.6 shows the values of the output voltage, inductor current and output current of the buck boost converter under constant duty cycle operation. The output voltage is seen to be an inverted reflection of the PV input voltage, which confirms proper operation of the buck boost converter at duty cycle 0.5. According to the inductor current, the buck boost converter is operating in continuous conduction mode with the current ripple of about 5A. The DC output current, output voltage and the inductor current are all seen to change proportionally to the changes in input PV current and voltage caused by changes in environmental conditions.

4.1.2 Simulation Under MPPT Operation

The second part of the isolated DC simulation involved testing the operation and performance of the perturb and observe maximum power point tracking algorithm with the buck boost converter. In this study a fixed step size P&O algorithm was implemented. The duty cycle perturbation step size was 0.01. The P&O algorithm was implemented with a delay time of 0.05 seconds to avoid perturbation of the duty cycle during the transient state of the system when oscillations are high. In order to shorten the convergence time of the maximum Power point tracking algorithm, the initial parameters of the system were set to: a voltage value of 490V, equal to the PV voltage under operation with duty cycle 0.5 as seen earlier; the duty cycle was set to 0.5 and the PV power was set to an arbitrary 1,490W. These settings are shown in Figure 4.7 ,which is a representation of the P&O algorithm using the Matlab-Simulink chart function. The simulation model setup for this stage is presented in appendix A.2.

From figure 4.8 it can be seen that the MPPT algorithm, in search for the maximum power point under rated irradiation and temperature, reduces the PV voltage from 490 V corresponding to constant duty cycle operation as seen earlier on to an oscillating average of around 400 V, while the PV current is increased from 4.2 A to an average fluctuating around 15 A. The oscillating nature of the PV parameters and the MPPT operation are due to the algorithm continuously monitoring the power and changing the duty cycle around the maximum power point as discussed in chapter 2. At time 0.9 seconds when the irradiation drops from $1{,}000W/m^2$ to $600W/m^2$, it can be seen that the PV current is affected the most, while on the other hand the effects of the subsequent changes in temperature are more visible in voltage.

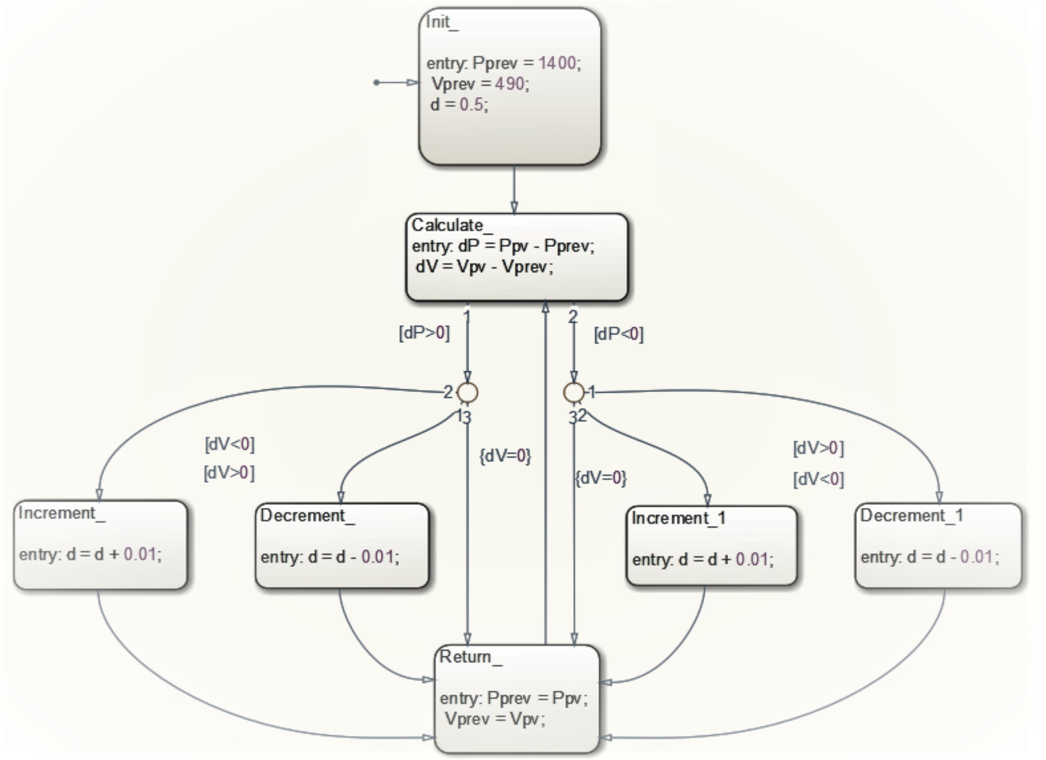

Figure 4.7 Perturb & Observe MPPT algorithm in Matlab Simulink

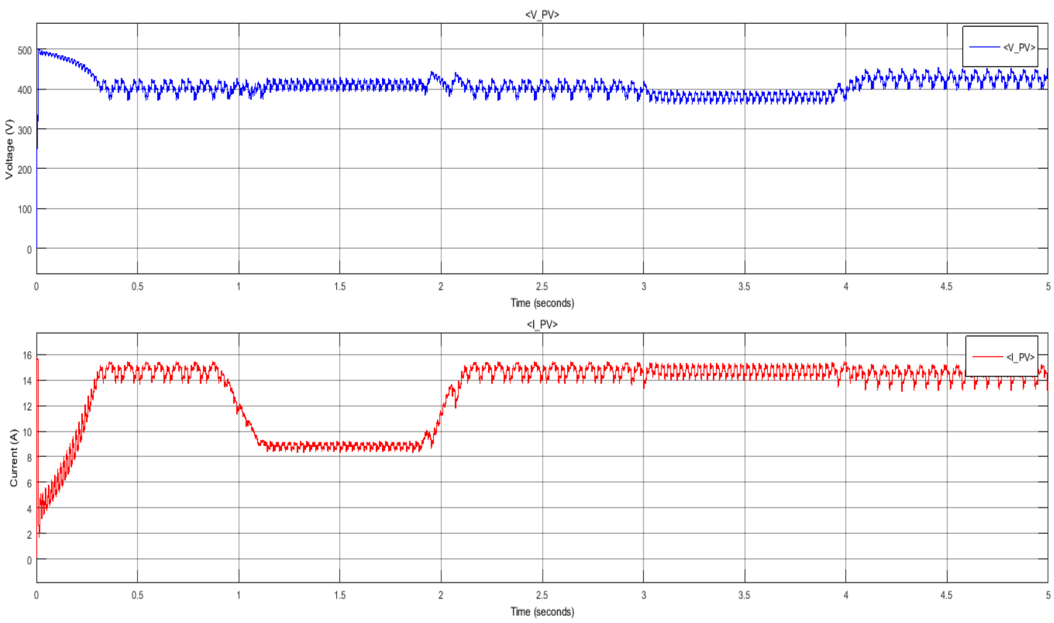

Figure 4.8 PV voltage and current under with MPPT operation

Figure 4.9 is a plot of the available PV power under MPPT operation against the

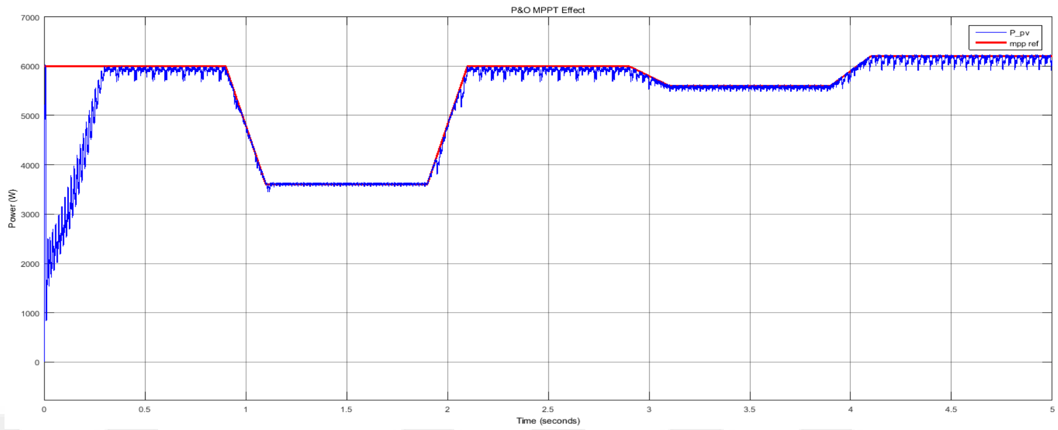

Figure 4.9 Available PV power under MPPT operation

reference maximum power signal generated according to the manufacturer's data. From this plot it can be seen that the buck boost converter operation with the maximum power point tracking algorithm successfully tracks the maximum power of the PV array under all conditions of irradiance and temperature. The convergence time of the algorithm was around 0.3 seconds.

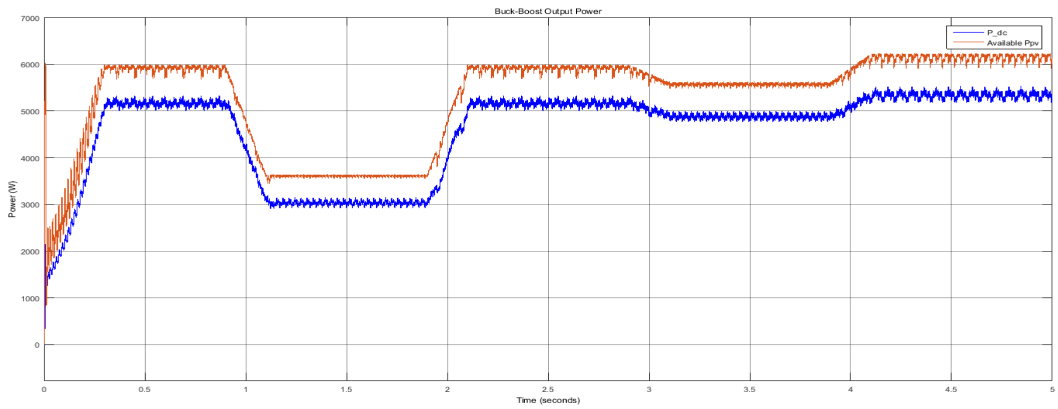

Figure 4.10 Buck-Boost converter output power under MPPT operation

Figure 4.10 shows a comparison of the power available from the PV array in the power available at the output of the buck boost converter. The maximum power available at the rated conditions of 25°C and $1{,}000 W/m^2$ is around 6 kW of the converter outputs 5.3 kW. In the second stage, when the irradiation decreases the expected maximum is 3.6 kW by the converter outputs 3kW. The efficiency of the system in all the cases is 88.33%. In figure 4.9 and figure 4.10 it can be seen that the PV array produces more power at 15°C as compared to the rated 25°C. This observation shows that the PV array is more efficient in cooler temperatures with high irradiation.

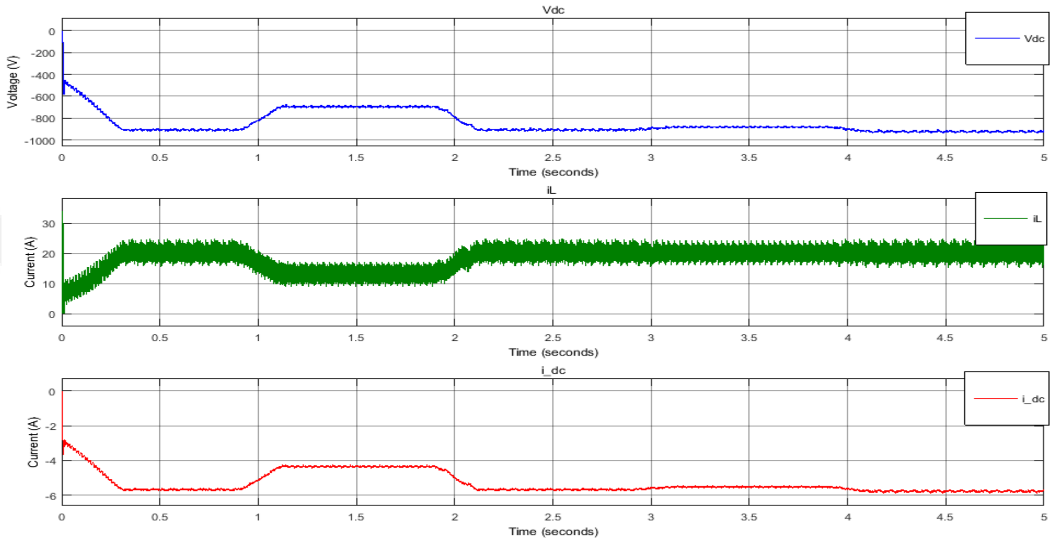

Figure 4.11 Buck-Boost output voltage, inductor current and output current under MPPT operation (a)

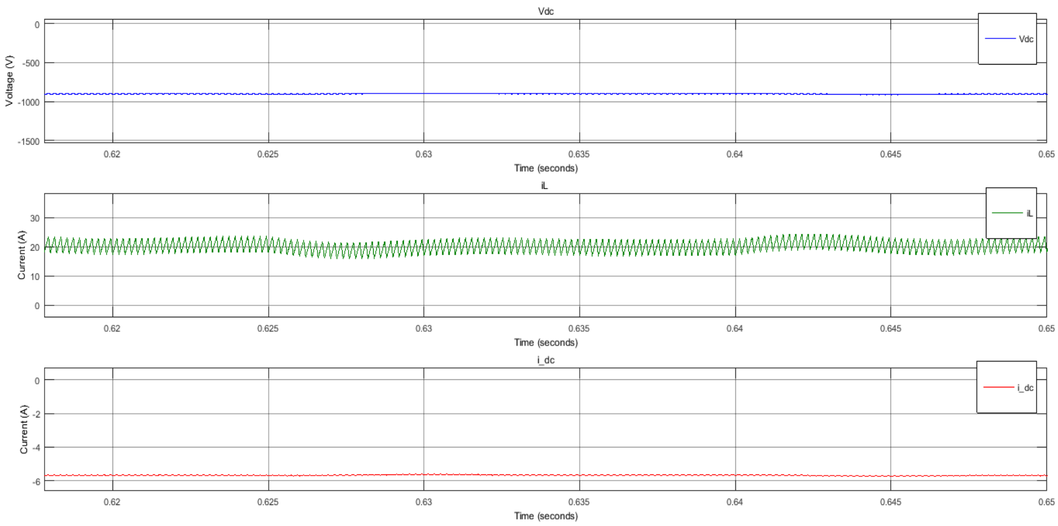

Figure 4.12 Buck-Boost output voltage, inductor current and output current under MPPT operation (b)

Figure 4.11 and figure 4.12 show the output voltage inductor current and output current of the buck boost converter in MPPT operation. As compared to constant duty cycle operation, at rated conditions the output voltage and current of the converter are boosted inverted values of around -900V and -5.88A. The inductor current is an average value of around 20A with an 8A ripple in continuous conduction mode. The inherent fluctuations caused by the P&O algorithm are also present in these waveforms.

Simulation of the isolated DC stage showed that the buck boost converter works well the perturb and observe algorithm in maximum power extraction from the PV array.

4.2 Simulation of Combined DC-AC Two-Stage Power Source

In this case, the photovoltaic DC stage was connected to the single phase voltage source inverter in conjunction with the LCL filter and an RL load is placed at the output of the two-stage system. The simulation of this system also involved an investigation of the effectiveness of the proposed modified PID controller as compared to the proportional resonant (PR) controller. The required voltage at the output of the system was considered to be 240 VAC.

The system was simulated in three modes: open-loop operation, closed-loop operation with the PID controller, closed-loop operation with a PR controller. Similarly, environmental conditions were varied in order to assess how changes in the primary power stage affect the output parameters of the system. Using information obtained from the small signal stability analysis in chapter 3, particularly the step response of the buck boost converter, which had a settling time of 0.095 seconds, the initial coupling of the two converters was timed to 0.15 seconds using a circuit breaker to connect them after the first stage has reached its steady state. The simulation model of the two-stage system is presented in appendix A.2.

Environment: At the time t = 0 seconds, the irradiance is $1{,}000W/m^2$ and the temperature is 25°C. The expected maximum power under these conditions is 6000W. From time t = 0.9 seconds to t = 1.1 seconds the irradiation drops from $1{,}000W/m^2$ to $600W/m^2$ while temperature is kept constant. From time t = 1.1 seconds to t = 1.9

seconds the environmental conditions are maintained and the expected maximum power is 3,600W. From time t = 1.1 seconds to t = 2.1 seconds the irradiance level is brought back up to 1,000W/m^2 and the temperature remains the same. At t = 2.9 seconds the temperature is increased from 25°C to 40°C, where it is maintained from time t = 3.1 seconds up to time t = 3.9 seconds. In this period the irradiance is maintained at 1,000W/m^2. The expected maximum power at this point is 5,600W. From time t = 3.9 seconds to time t = 4.1 seconds the temperature is dropped from 40°C to 15°C, with the irradiation being kept at 1,000W/m^2. Under these conditions, the expected maximum power of the PV array is 6,200W. At the 5s mark the simulation is stopped.

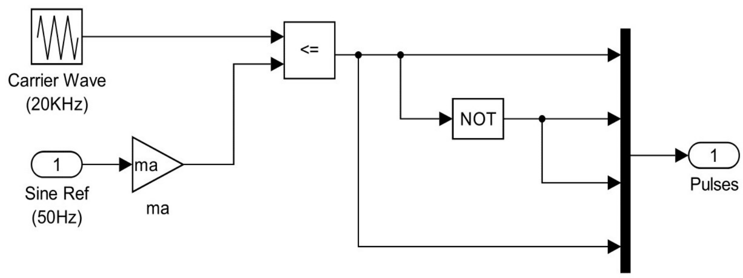

Figure 4.13 Simulink bipolar PWM implementation

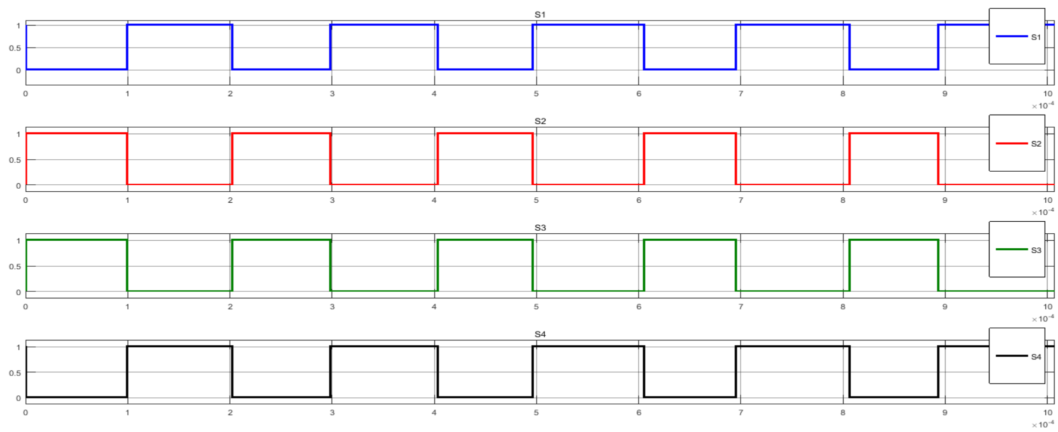

Figure 4.14 PWM gate signals

The bipolar pulse width modulation technique using a carrier wave of frequency 20 kHz was used to operate the inverter in the second stage. Figure 4.13 shows the implementation of the bipolar PWM in Simulink and figure 4.14 shows the gate signals to the switches S1, S2, S3, S4.

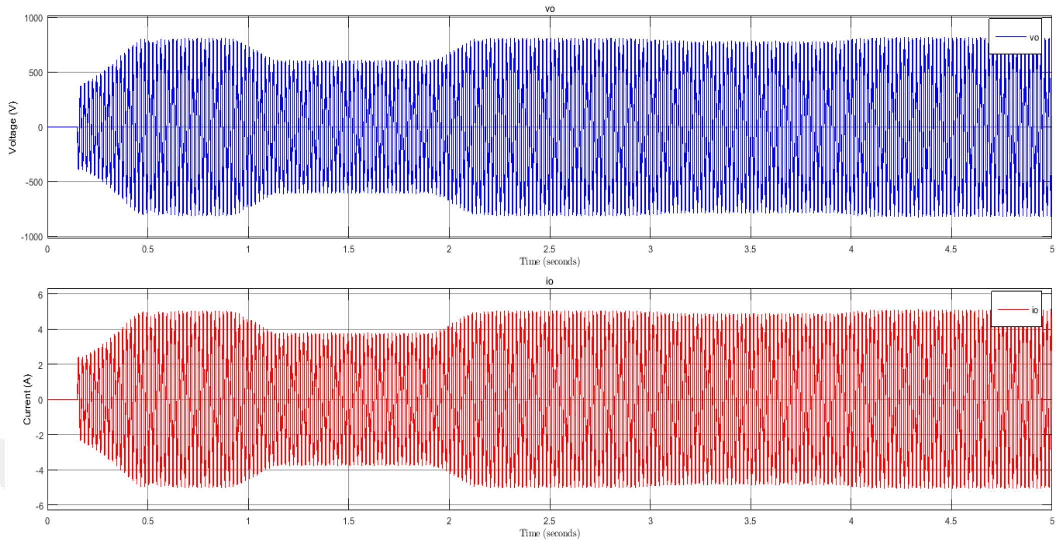

Figure 4.15 Inverter output voltage and current in open-loop operation with RL load

Figure 4.15 shows the uncontrolled output voltage and current of the inverter. It can be seen that is environmental conditions change, the DC link voltage changes and so does the amplitude of the output voltage and current of the inverter.

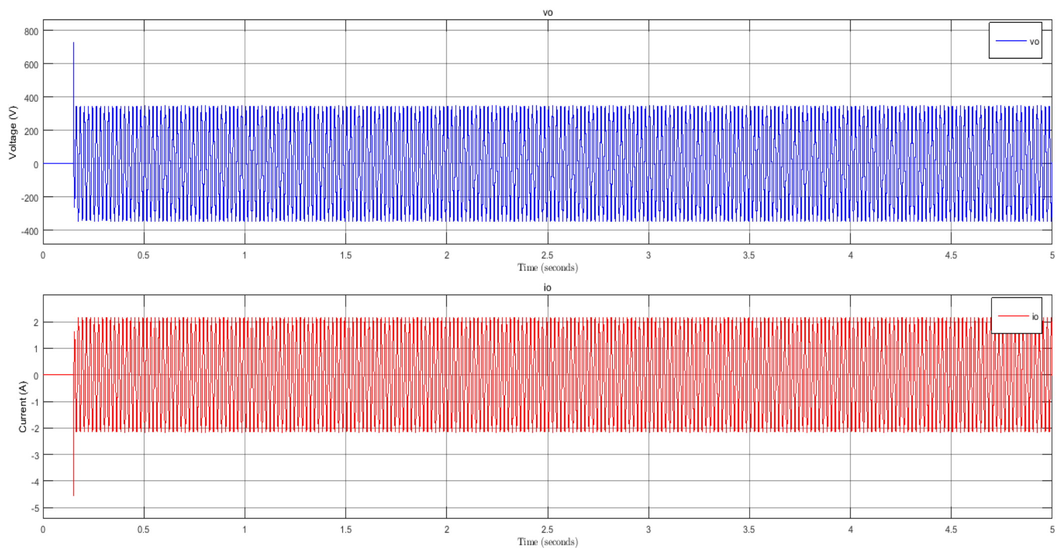

Figure 4.16 Inverter output voltage and current with PID voltage-oriented control (a)

Figure 4.16 shows the controlled output voltage and current of the inverter using the PID controller. The amplitude of the output parameters is seen to remain constant

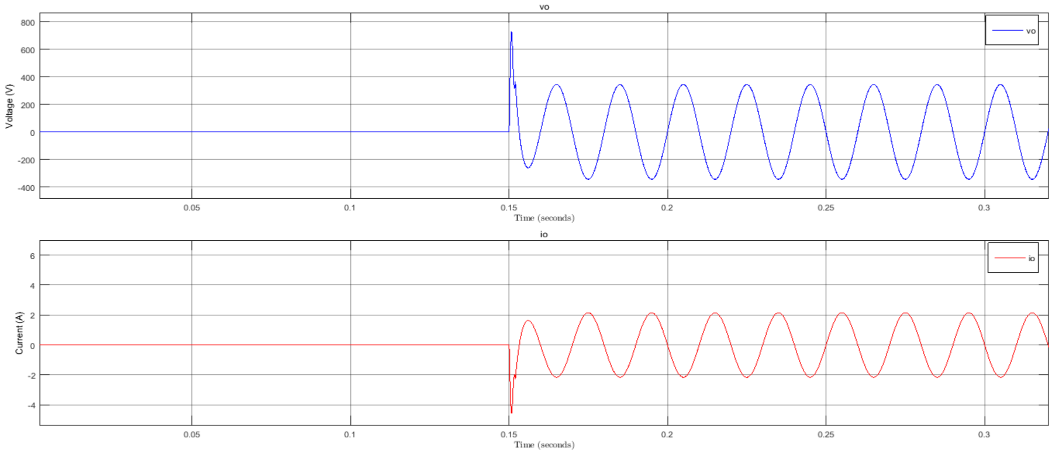

Figure 4.17 Inverter output voltage and current with PID voltage-oriented control (b)

throughout the simulation. However, as seen in figure 4.17, the PID controller exhibits parameter overshoot at the coupling moment by the circuit breaker. This overshoot is seen to have effects throughout the system up until the PV array as seen in figure 4.20 and figure 4.21.

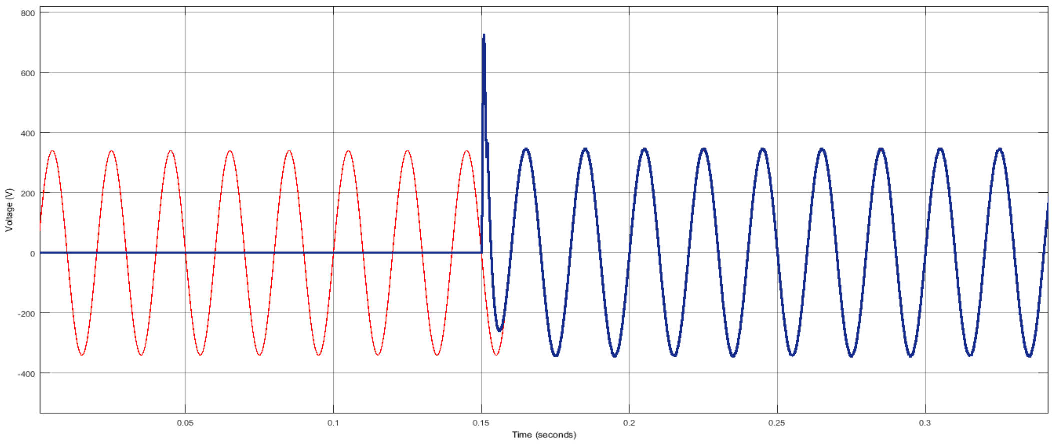

Figure 4.18 Inverter output voltage vs reference voltage with PID controller

Figure 4.18 is a plot of the output voltage of the inverter using a PID controller against the reference voltage signal. Despite the voltage surge at the moment of coupling, the PID controller was capable of tracking the reference signal perfectly, with the total harmonic distortion (THD) of the output voltage waveform being only 0.5%.

Figure 4.22 and figure 4.23 show the plots of the output voltage and current of the inverter using a PR controller the amplitude of the output parameters remains constant

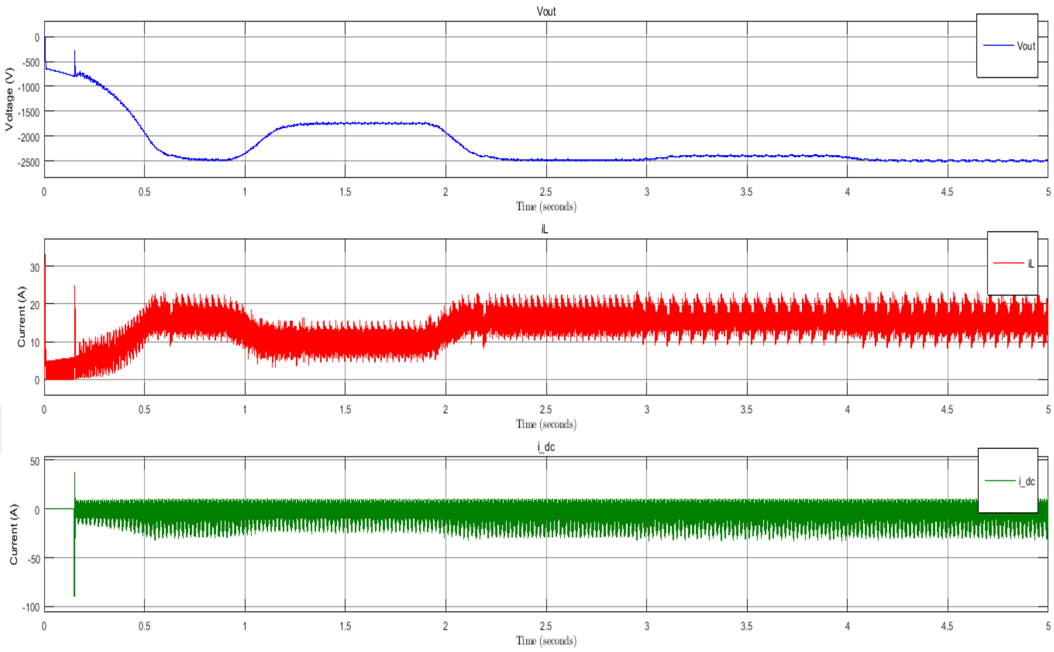

Figure 4.19 Buck-Boost converter output voltage, inductor current and DC-link current with PID controller (a)

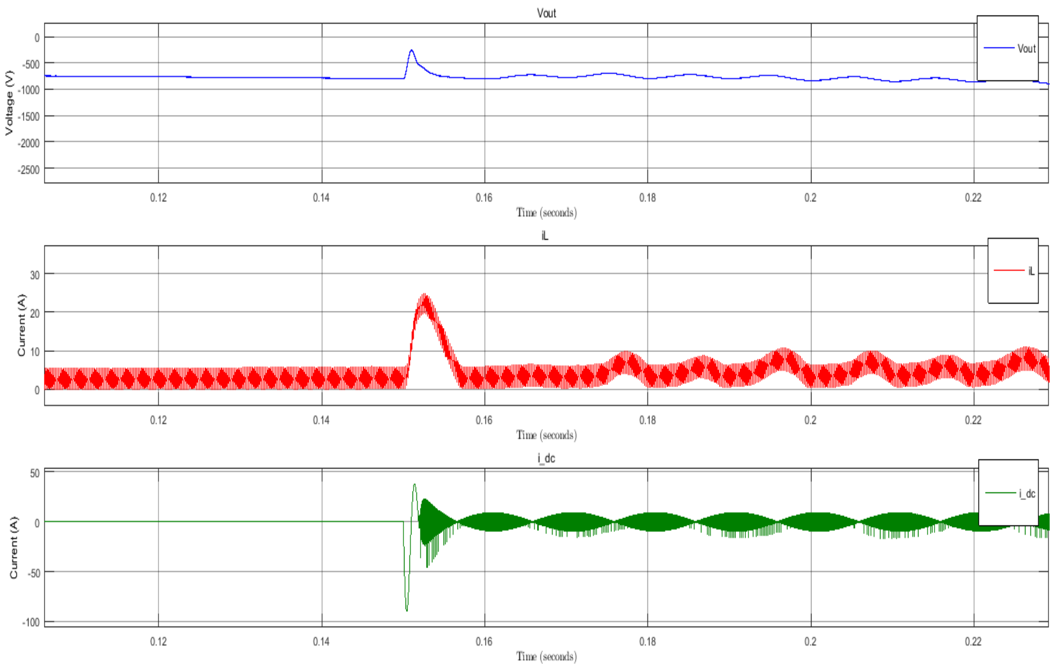

Figure 4.20 Buck-Boost converter output voltage, inductor current and DC-link current with PID controller (b)

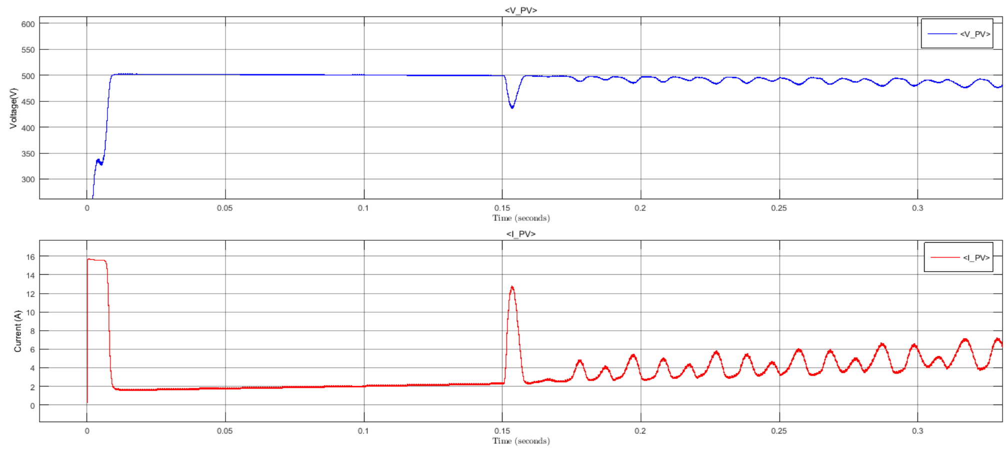

Figure 4.21 PV voltage and current when system is operated with PID controller

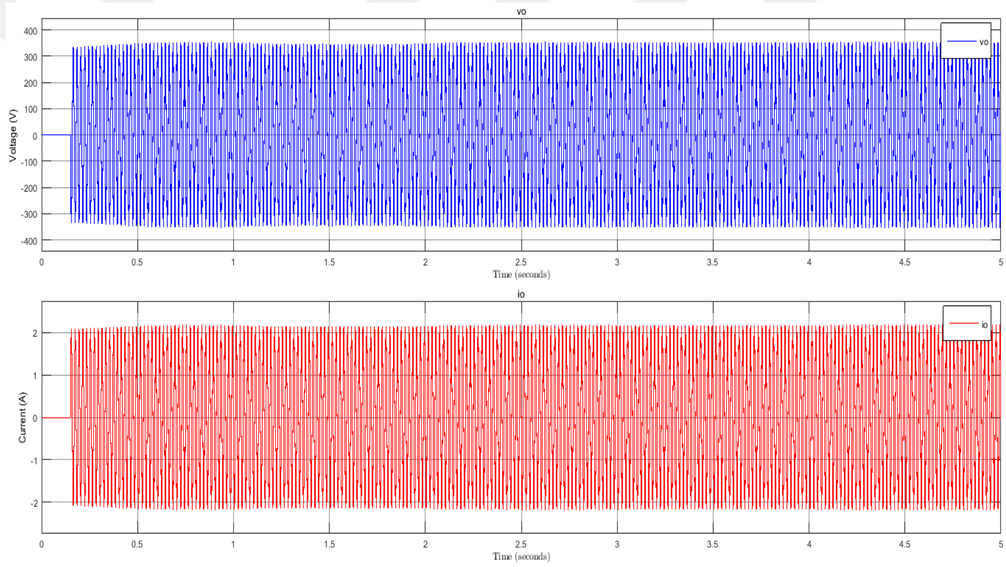

Figure 4.22 Inverter output voltage and current with PR voltage-oriented control (a)

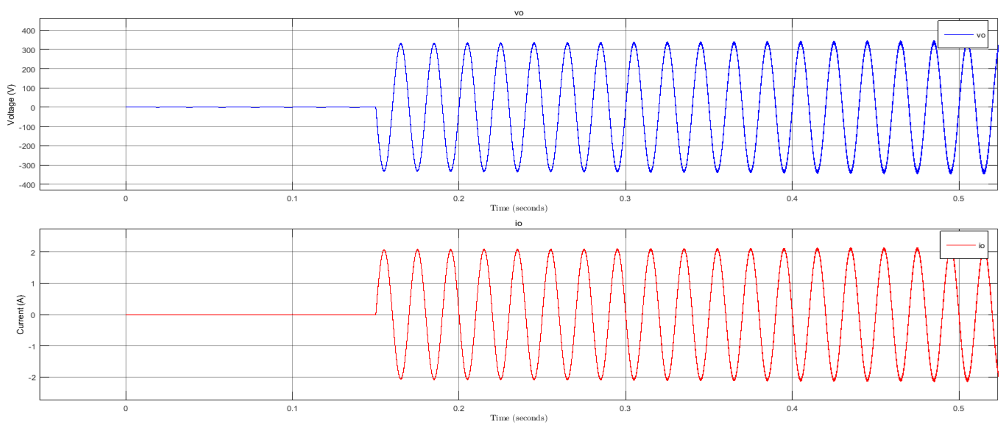

Figure 4.23 Inverter output voltage and current with PR voltage-oriented control (b)

throughout the simulation, and unlike in the case of the PID controller, no overshoot was observed.

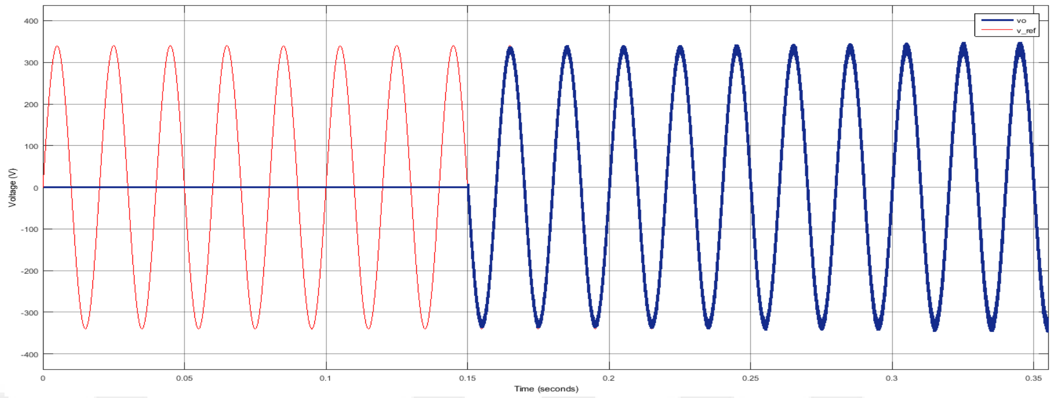

Figure 4.24 Inverter output voltage vs reference voltage with PR controller

Figure 4.24 shows the plot of the output voltage of the inverter using a PR controller against the reference voltage signal. The PR controller is seen to track the voltage reference perfectly, with a total harmonic distortion (THD) of 2.65%.

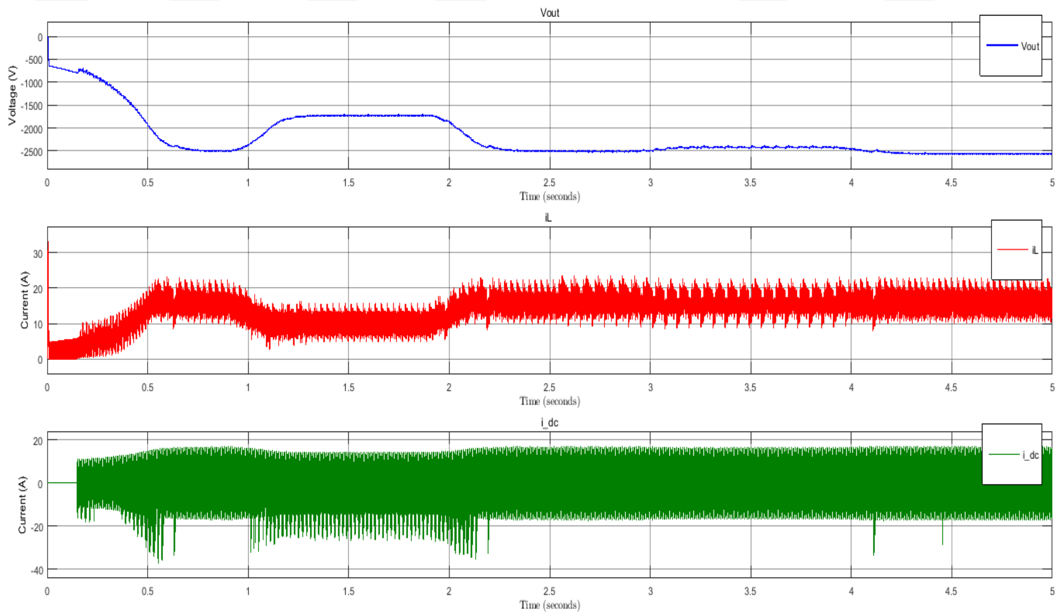

Figure 4.25 Buck-Boost converter output voltage, inductor current and DC-link current with PR controller (a)

Figure 4.25 in figure 4.26 show the buck boost converter output voltage, the inductor current and the DC link current when the inverter is operated with a PR controller. The

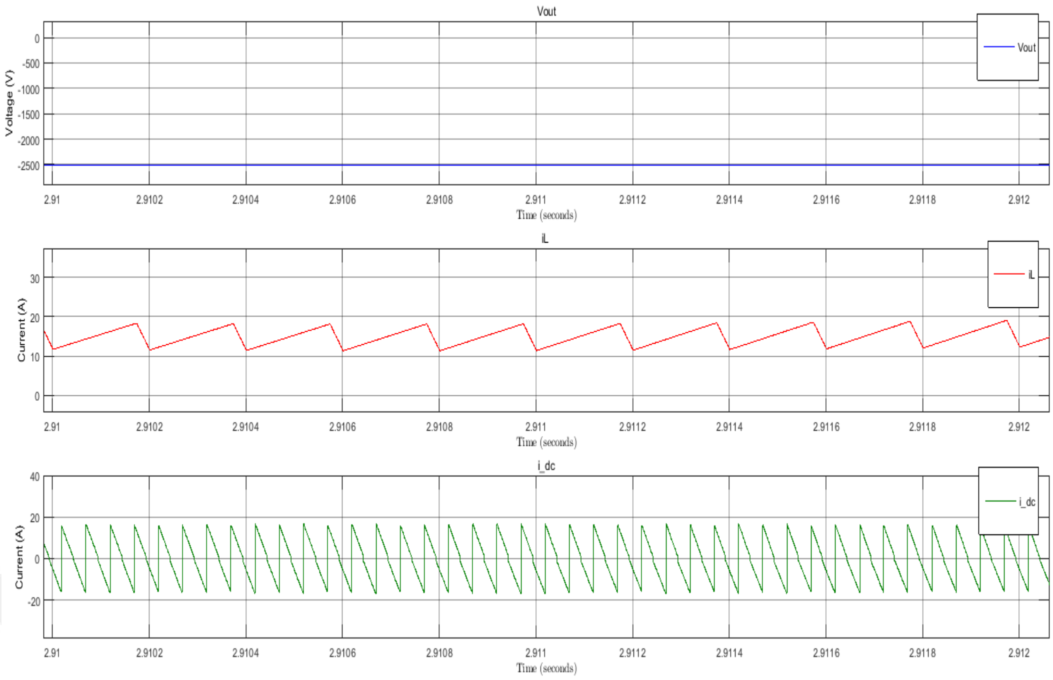

Figure 4.26 Buck-Boost converter output voltage, inductor current and DC-link current with PR controller (b)

buck boost converter, as before, operates in continuous conduction mode.

4.3 Simulation of Complete Photovoltaic Pumping System with BLDC Load

In this section , the simulation of the complete two-stage PV pumping system with a BLDC motor is presented. The photovoltaic DC stage is connected to the single phase voltage source inverter coupled with the LCL filter as in the previous section but in this case, the RL load is replaced by an integrated AC input BLDC motor drive. The AC output from the two-stage power source is fed to the integrated rectifier circuit which converts it to a constant average DC voltage. This DC value appears across the terminals of the inverter in the drive circuit. The simulation of this system also involved observing the effectiveness of the proposed PID controller in comparison to the PR controller when connected to a rectifier at the load. Environmental conditions were set to 1,000W/m^2 irradiance and 25°C temperature. The pump drive is set to operate with a reference speed of 300 rad/s and the mechanical load is set at a constant reference of 10Nm. The Matlab Simulink BLDC drive model and complete system simulation setup are presented in appendix A.2.

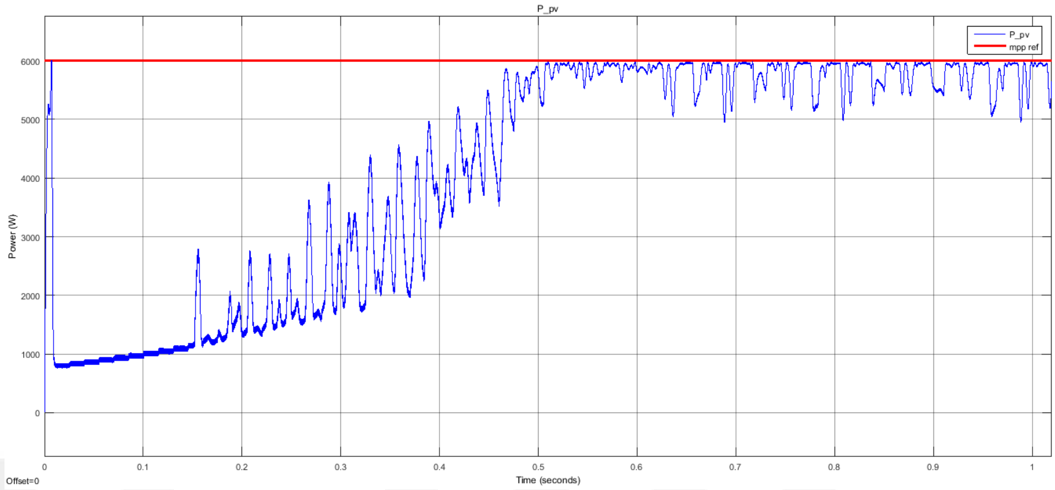

Figure 4.27 Available PV power when complete system is operated at 1,000W/m^2 and 25°C

Figure 4.27 shows the available PV power when the complete system is operated under rated environmental conditions. It can be seen that with MPPT operation, the power still oscillates and values around the maximum power point i.e. 6 kW. Figure 4.28 shows the corresponding PV voltage in PV current plots. Figure 4.29 shows the waveforms of the buck boost converter output voltage, inductor current and DC link current.

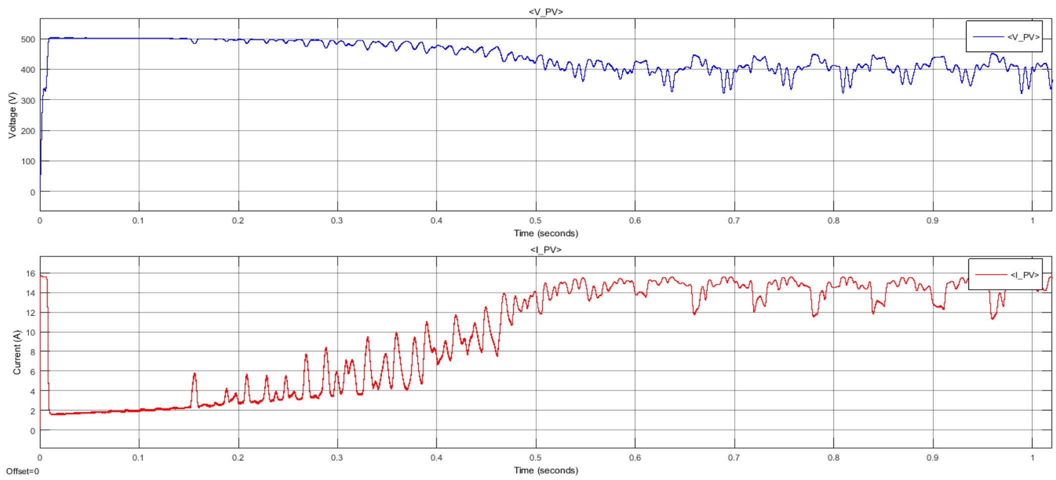

Figure 4.28 PV voltage and current when complete system is operated at 1,000W/m^2 and 25°C

Figure 4.30 shows the characteristics of the BLDC motor drive under this set out

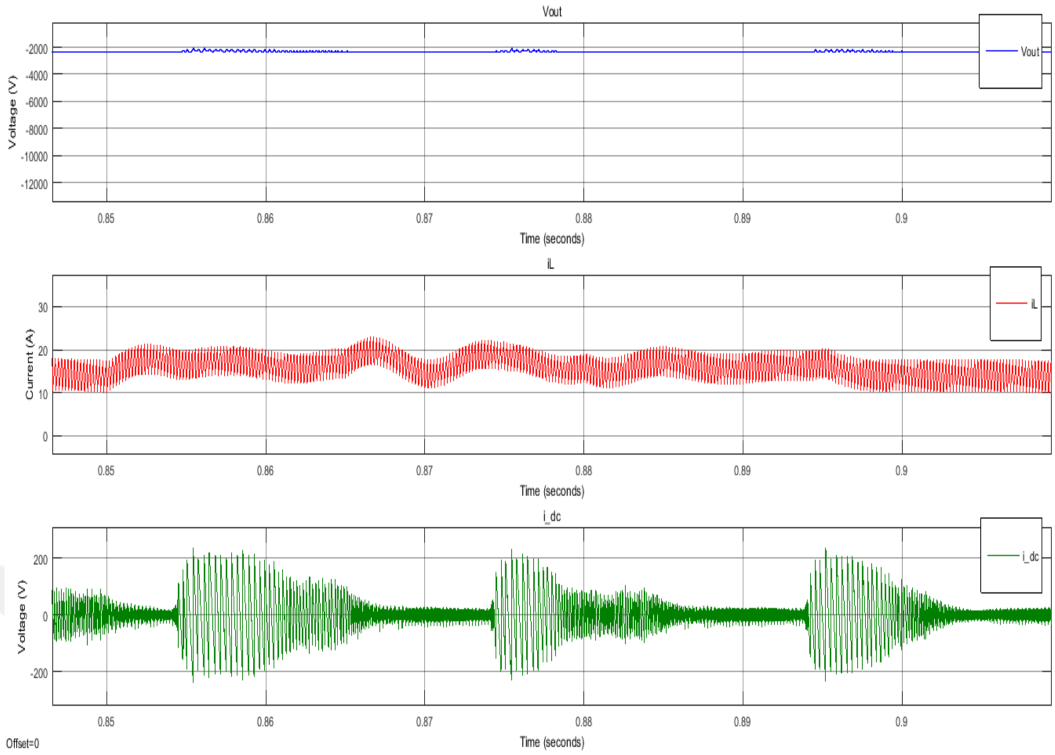

Figure 4.29 Buck-Boost converter output voltage, inductor current and DC–link current with BLDC drive

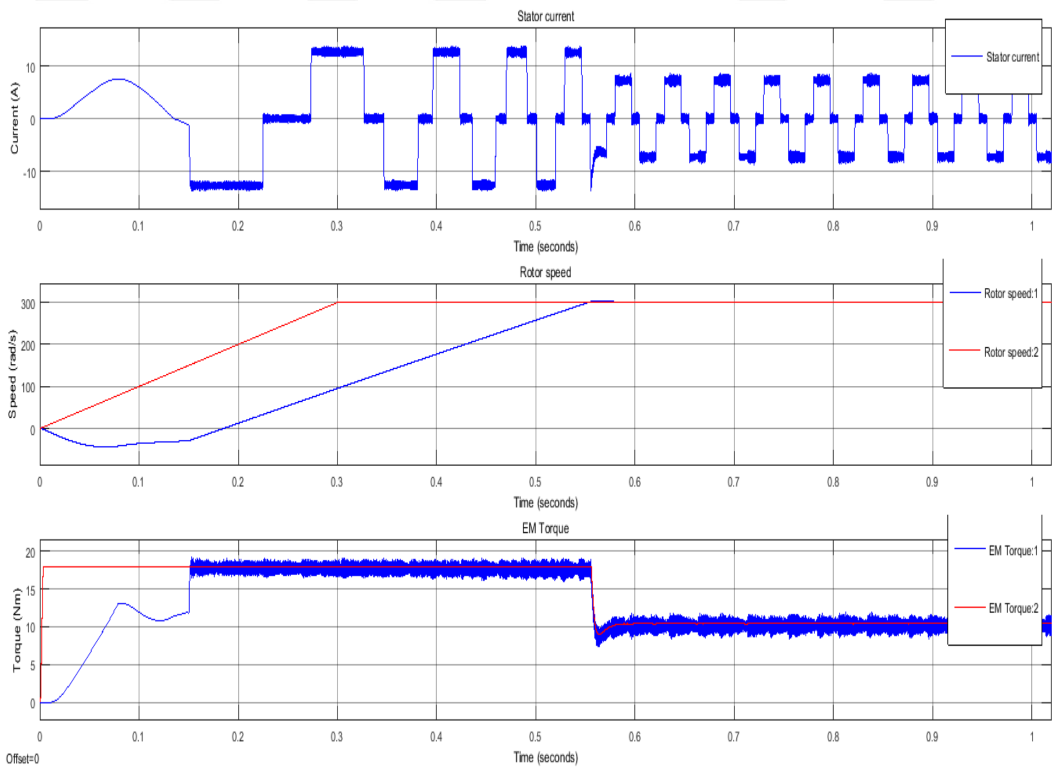

Figure 4.30 BLDC drive stator current, speed and electromagnetic torque simulation results

operational conditions. (From top to bottom) The first plot represents the BLDC motor stator current, the second plot shows the rotor speed against its reference, the third characteristic shows the BLDC motor electromagnetic torque against its reference. The operation of the two-stage PV system in the simulation was kept the same i.e. power is fed into the secondary stage after 0.15 seconds through the coupling circuit breaker. As seen from the characteristics, before time 0.15 seconds, the BLDC motor is under the action of the applied constant load torque. When the switch is closed at time 0.15s the rotor speed starts to increase linearly towards its reference value. In this accelerating period the stator current and torque is high. The rotor speed catches up to the reference value of 300rad/s around time 0.55 seconds, and at this time the electromagnetic torque equals the reference load torque.

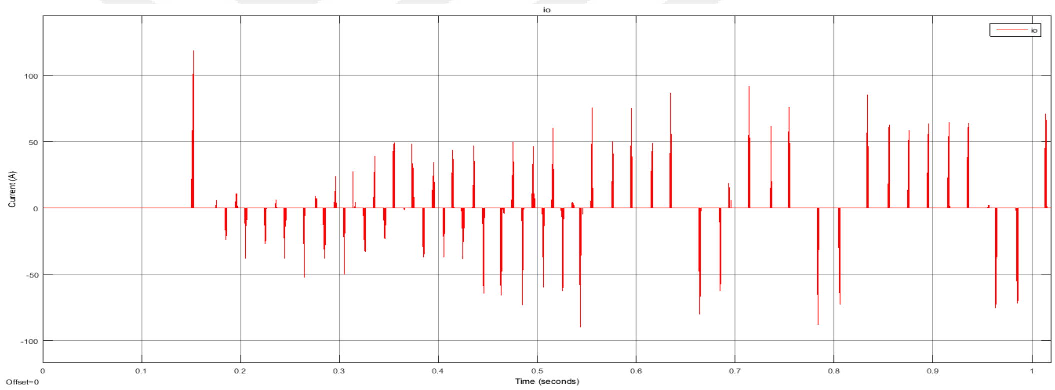

Figure 4.31 BLDC drive rectifier input current

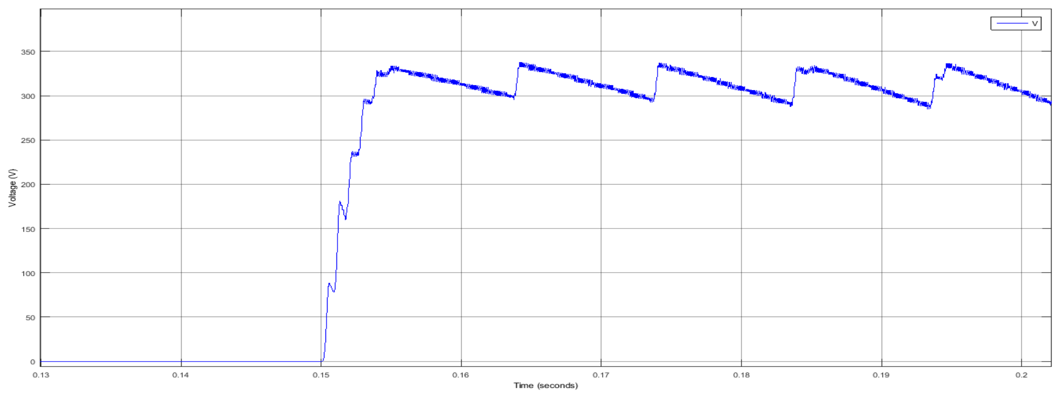

Figure 4.32 BLDC drive rectifier output voltage

Figure 4.33 shows the output voltage of the inverter which feeds the BLDC drive

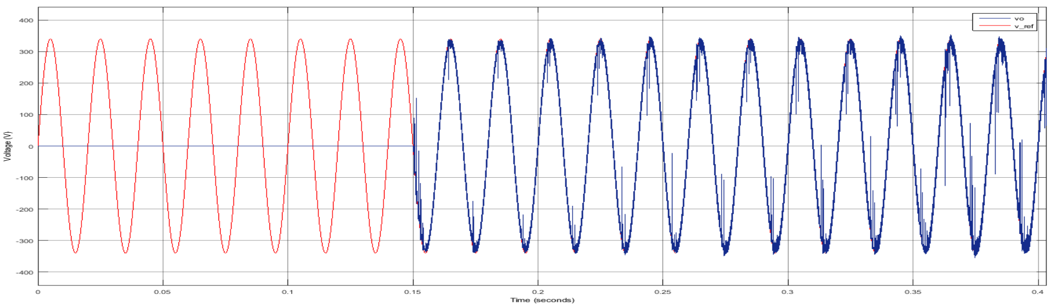

Figure 4.33 Inverter output voltage when operated with BLDC drive and PR controller

rectifier when regulated by a PR controller. The total harmonic distortion (THD) observed in this case was around 8.5%

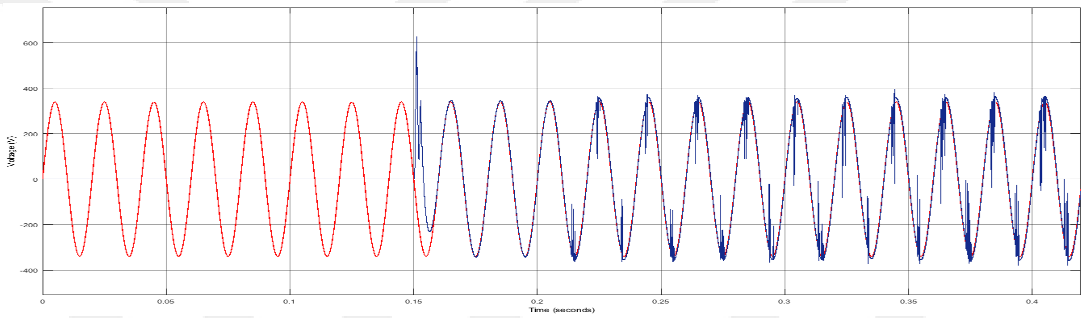

Figure 4.34 Inverter output voltage when operated with BLDC drive and PID controller

Figure 4.34 shows the output voltage of the inverter which feeds the BLDC drive rectifier when regulated by a PID controller. The total harmonic distortion (THD observed in this case was around 11.8%

From the simulation the complete model ,it is seen that all components of the proposed two-stage pumping system operating correctly: The first stage successfully extracts maximum power from the PV array using the P&O algorithm with the buck boost converter, the second stage achieves voltage regulation to meet the requirements the motor drive, and the BL DC motor drives functions properly with speed control.

System parameters evaluated and used for simulations presented in these sections are provided in table 4.1.

Table 4.1 Parameters

Buck Boost Converter	Inductor, L = 10mH
	DC-link capacitor, C = 100uF
	Switching frequency, f_s= 5kHz
LCL Filter	Inverter side inductance, L_1= 2mH
	Load side inductance, L_2= 0.5mH
	Filter capacitance, C_f= 80uF
	Damping resistance, r_d= 3 Ohms
Loads	Resistive load, R = 160 Ohms
	Inductive load, L = 1mH
	BLDC = 3kW
Inverter	Switching frequency, f_s= 20kHz
	m_a= 1
	Line f_n= 50Hz
PID controller	K_p= 18.4863
	K_i= 1,0000
	K_d= 0.0090965
PR controller	K_r= 0.0005
	K_p=0.05

CHAPTER FIVE
CONCLUSIONS

This thesis presented the design and investigation of a proposed two-stage standalone photovoltaic system to power a brushless DC (BLDC) motor – pump. The proposed system consisted of a primary DC stage comprising of the PV array and an interfacing Buck-Boost DC-DC converter for maximum power extraction, as well as a secondary AC stage in the form of a single-phase full bridge voltage source inverter whose output voltage was controlled to match the required input to the BLDC drive.The study reviewed the fundamentals and the main design considerations for the system, based on which the system was modeled and simulated.

The results from the simulation show that the buck boost converter is capable of stable operation with the direct duty cycle perturbation MPPT algorithm. Using the Buck boost converter and the perturb and observe algorithm the total power available from the PV array was seen to match the MPP values as given by the manufacturer for all irradiance and temperature levels that were investigated. The overall efficiency of the DC power stage was seen to be around 88%. In conclusion, the buck boost converter is suitable for maximum PowerPoint tracking applications. This converter topology is stable in the entire region of voltage – current characteristics of the PV modules.

Voltage control was achieved at the second stage of the system using the proportional resonant controller as well as the PID controller. When simulated with an RL load, the proposed PID controller showed a higher level of harmonic attenuation in steady state operation as compared to the PR controller, i.e. 0.5% versus 2.65% respectively, however, the system showed a large overshoot at the moment when the circuit breaker connecting these two stages was closed. The PR controller on the other hand, is capable of following the reference voltage without any initial spikes. Additionally, when the complete system including the BLDC motor drive was simulated, the PR controller showed to be more robust than the PID controller with a rectifier at the load terminal as the total harmonic distortion in the inverter output voltage rose to around 8.5% for the PR controller as compared to 11.8% for the PID controller. Can be concluded that both controllers if well designed are capable of regulating the voltage in the required range, with the PR controller being the more robust option.

Overall, the proposed two-stage system achieved the two objectives of this study, namely maximum power extraction in the DC stage and voltage regulation in the AC stage to successfully run the BL DC pump drive.

For future studies, I propose the behavioural analysis of the two-stage solar PV system using a complete system mathematical model, combining all components: the PV array, the DC to DC converter, the DC to AC inverter and the load. This approach may provide better information about the dynamics of the system as a whole, leading to a better design.

REFERENCES

Amine A., Ouassaid M., Maaroufi M (2013). Modified p&o mppt technique for photovoltaic systems. *International Conference on Renewable Energy Research and Applications*, 728- 733.

Aström K. J. (2002). Control system design lecture notes for me 155a. *Department of Mechanical and Environmental Engineering University of California Santa Barbara*, 1-333.

Chandrasekaran N., Ganeshprabu B., Thyagarajah K. (2012). Matlab based comparative study of photovoltaic fed dc motor and pmdc motor pumping system. *ARPN Journal of Engineering and Applied Sciences*, *7*(5), 543-547.

Elgendy M., Zahawi B., Atkinson D. (2012). Assessment of perturb and observe mppt algorithm implementation techniques for pv pumping applications. *IEEE Transactions on Sustainable Energy*, *3*(1), 21-33.

Elgendy M., Zahawi B., Atkinson D. (2013). Comparison of directly connected and constant voltage controlled photovoltaic pumping systems. *IEEE Transactions on Sustainable Energy*, *1*(3), 184-192.

Femia N., Petrone G. (2005). Optimization of perturb and observe maximum power point tracking method. *IEEE Transactions on Power Electronics*, *20*(4), 963-973.

Guerrero J., Luis G., Castilla M. (2005). Output impedance design of parallel-connected ups inverters with wireless load-sharing control. *IEEE Transactions on Industrial Electronics*, *52*(4), 1126-1135.

Guerrero X., Romero J., Carangui X. (2016). Power electronics and control techniques for maximum energy harvesting in photovoltaic systems. *51st International Universities Power Engineering Conference (UPEC)*, *5*, 66-67.

Hafezi H., Akpınar E., Balıkçı A. (2014). Cascade pi controller for single-phase statcom. *16th International Power Electronics and Motion Control Conference and Exposition*, 88-93.

Hosseini S., Farakhor A., Haghighian S. (2013). Novel algorithm of maximum power point tracking (mppt) for variable speed pmsg wind generation systems through model predictive control. *International Conference on Electrical and Electronics Engineering (ELECO)*, 243- 247.

IRENA (2019). Future of solar photovoltaic: Deployment, investment, technology, grid integration and socio-economic aspects (a global energy transformation: paper). *International Renewable Energy Agency, Abu Dhabi*, 1-73.

Jubaer A., Zainal S. (2018). An enhanced adaptive p&o mppt for fast and efficient tracking under varying environmental conditions. *IEEE Transactions on Sustainable Energy*, *9*(3), 1487-1496.

Kakosimos P. E., Kladas A., Manias S. (2013). Fast photovoltaic-system voltage- or current-oriented mppt employing a predictive digital current-controlled converter. *IEEE Transactions on Industrial Electronics*, *60*(12), 5673-5685.

Kinas J., Acevedo-Bueno D. et al. (2018). Comparative evaluation of modulation strategies for a single- phase pv micro-inverter with high-frequency transformer. *IEEE Applied Power Electronics Conference and Exposition (APEC)*, 3238-3243.

Kumar R., Singh B. (2014). Solar pv array fed water pumping system using sepic converter based bldc motor drive. *Eighteenth National Power Systems Conference (NPSC)*, 1- 5.

Kumar R., Singh B. (2016). Bldc motor-driven solar pv array-fed water pumping system employing zeta converter. *IEEE Transactions on Industry Applications*, *52*(3), 2315- 2322.

Maissa F., Barambones O., Sbita L. (2016). A real-time implementation of mppt-based on p&o method. *5th International Conference on Electronic Devices, Systems and Applications*, 1-5.

Narasimharaju B., Goutham B., Vijay B., Ramanjaneya R. (2015). Modeling and analysis of voltage controlled positive output synchronous buck-boost converter. *IEEE INDICON*, 1-5.

Narayana A., Raju P., Ramana K. (2018). Proportional resonant controller with resonant harmonic compensators for three-phase multilevel inverter. *International Research Journal of Engineering and Technology (IRJET)*, *6*, 812-816.

Paja C., Petrone G., Montes A., Julián S. (2012). Compensation of dc-link voltage oscillations in grid connected pv systems. *IEEE International Symposium on Alternative Energies and Energy Quality (SIFAE)*, 82-92.

Raja R., Nagarajan C., Sudha V. (2016). Designing of lcl filter and stability analysis of a three phase grid connected inverter system. *International Journal of Science, Engineering and Technology Research (IJSETR)*, *5*(1), 306-312.

Sahoo A., Shahani A., Basu K., Mohan N. (2014). Lcl filter design for grid-connected inverters by analytical estimation of pwm ripple voltage. *Applied Power Electronics Conference and Exposition - APEC*, 1281-1286.

Salem M., Atia Y. (2015). Control scheme towards enhancing power quality and operational efficiency of single-phase two-stage grid-connected photovoltaic systems. *Journal of Electrical Systems and Information Technology*, 2 314–327.

Scortegagna A., Leite V., Roman D. (2019). New approaches for low power photovoltaic water pumping systems. *45th Annual Conference of the IEEE Industrial Electronics Society - IECON*, 2270-2275.

Teodorescu R., Blaabjerg F., Liserre M. (2004). Proportional-resonant controllers. a new breed of controllers suitable for grid-connected voltage-source converters. *9th International Conference on Optimization of Electrical and Electronic Equipments*, 9-14.

Yoon D., Jeong H., Lee K. (2010). The design of an lcl-filter for the three-parallel operation of a power converter in a wind turbine. *IEEE Energy Conversion Congress and Exposition*, 1537-1544.

Zhang N., Tang H., Yao C. (2014). A systematic method for designing a pr controller and active damping of the lcl filter for single-phase grid-connected pv inverters. *Energies*, 3934-3954.

APPENDICES

A.1: MATLAB Code for Averaged Small Signal Modelling of Buck-Boost Converter

Small Signal Function

```
function [Gy_u, Gy_d] = mugwamba_smallsignalfunction(mA,mB,mC,mD,X,U,Y)

%% Definition of the duty cycle vector
    syms d
    md = [d 1-d];

%% Small Signal Average Modeling
Am = 0; Bm = 0; Cm = 0; Dm = 0;

for i = 1:length(mA)
    Am = Am + (mA{i}*md(i));
    Bm = Bm + (mB{i}*md(i));
    Cm = Cm + (mC{i}*md(i));
    Dm = Dm + (mD{i}*md(i));
end

Am = simplify(Am); Bm = simplify(Bm); Cm = simplify(Cm); Dm = simplify(Dm);

%% Steady-state DC model  % All variables are average values
for i = 1:length(X{1})
    var = char(X{1}(i));
    Xdc(i,1) = sym(strcat(var,'_dc'));
end
for i = 1:length(Y{1})
    var = char(Y{1}(i));
    Ydc(i,1) = sym(strcat(var,'_dc'));
end
Xdc = -Am^-1*Bm*U;
Ydc = Cm*Xdc+Dm*U;

%% Small-signal model
syms S   %Laplace domain
[n,m] = size(Am);
for i = 1:length(X{1})
    var = char(X{1}(i));
```

```
    x_ss(i,1) = sym(strcat(var,'_ss'));
end

for i = 1:length(U{1})
    var = char(U{1}(i));
    if var == '0'
        u_ss(i,1) = sym(var);
    else
        u_ss(i,1) = sym(strcat(var,'_ss'));
    end
end

for i = 1:length(md)-1
    var = char(d(i));
    d_ss(i,1) = sym(strcat(var,'_ss'));
end

for i = 1:length(Y{1})
    var = char(Y{1}(i));
    y_ss(i,1) = sym(strcat(var,'_ss'));
end

x_ss=simplify(((S*eye(n,m)-Am)^-1)*(Bm*u_ss+((mA{1}-mA{2})*Xdc+(mB{1}
 -mB{2})*U)*d_ss));
y_ss=simplify(Cm*x_ss+Dm*u_ss+((mC{1}-mC{2})*Xdc+(mD{1}-mD{2})*U)*d_ss);

%% Transfer functions
% Variation of duty cycle (u_ss = 0)
zerosv = zeros(1,length(symvar(u_ss)));
y_ss_u0 = simplify(subs(y_ss,symvar(u_ss),zerosv));
G_ss_y_d = collect((y_ss_u0/d_ss),S);% Y_ss/d_ss transfer functions

% Variation of inputs (d_ss = 0)
for i = 1:length(u_ss)
   if u_ss(i) == symvar(u_ss(i))
   zerosv=zeros(1,length(symvar(u_ss)));
   y_ss_d0=simplify(subs(y_ss,[symvar(u_ss(u_ss~=u_ss(i))) d_ss],zerosv));
%duty cycle and irrelevant inputs = 0
       G_ss_y_u(:,i) = collect((y_ss_d0/u_ss(i)),S);
    else
        G_ss_y_u(:,i) = sym(0);
    end
end

Gy_u = G_ss_y_u;
```

```
Gy_d = G_ss_y_d;
end
```

Buck-Boost Converter Modeling

```
% Definition of symbolic variables
syms ron rL R rC d vd L C Iload iL vC Vin iin vo S Vm rm rl rc io Vd rd iout

%ON state
a11=-((rl+rm)/L); a21=0; a12=0; a22=-1/((R+rc)*C);
b11=1/L; b12=0; b13=-1/L; b14=0; b21=0; b22=-R/((R+rc)*C); b23=0; b24=0;
c11=0; c12=R/(R+rc); c21=0; c22=1/(R+rc); c31=1; c32=0;
d11=0; d12=-(R*rc)/(R+rc); d13=0; d14=0; d21=0; d22=R/(R+rc); d23=0;
d24=0; d31=0; d32=0; d33=0; d34=0;

A1=[a11 a12;a21 a22];
B1=[b11 b12 b13 b14;b21 b22 b23 b24];
C1=[c11 c12;c21 c22;c31 c32];
D1=[d11 d12 d13 d14;d21 d22 d23 d24;d31 d32 d33 d34];

%OFF state
A11=-((R*rc+R*rl+rl*rc+R*rd+rd*rc)/(L*(R+rc))); A12=-R/(L*(R+rc));
A21=R/(C*(R+rc)); A22=-1/((R+rc)*C);
B11=0; B12=(R*rc)/((R+rc)*L); B13=0; B14=-1/L; B21=0; B22=-R/((R+rc)*C);
B23=0; B24=0;
C11=(R*rc)/(R+rc); C12=R/(R+rc); C21=rc/(R+rc); C22=1/(R+rc); C31=1;
 C32=0;
D11=0; D12=-(R*rc)/(R+rc); D13=0; D14=0; D21=0; D22=R/(R+rc); D23=0;
D24=0; D31=0; D32=0; D33=0; D34=0;

A2=[A11 A12;A21 A22];
B2=[B11 B12 B13 B14;B21 B22 B23 B24];
C2=[C11 C12;C21 C22;C31 C32];
D2=[D11 D12 D13 D14;D21 D22 D23 D24;D31 D32 D33 D34];

Ap= A1*d + A2*(1-d); %Am
Bp= B1*d + B2*(1-d); %Bm
Cp= C1*d + C2*(1-d); %Cm
Dp= D1*d + D2*(1-d); %Dm

% Required cell matrices
mA = {A1;A2};
mB = {B1;B2};
mC = {C1;C2};
```

```
mD = {D1;D2};
X = {[iL;vC]};
U = {[Vin;Iload;Vm;vd]};
Y = {[vo;iout;iL]};

% Obtain the small-signal transfer functions
[Gy_u_bb, Gy_d_bb] = mugwamba_smallsignalfunction(mA,mB,mC,mD,X,U,Y)

% Substitute symbolic variables by numeric values
Parameters = [ron rL R rC vd L C Iload Vin d Vm rm];
Values = [10e-5 10e-5 160 10e-5 10e-5 0.01 0.0001 5 500 0.5 10e-5 10e-5];
% Substitute symbolic variables by numeric values
Gy_u_bb_num = collect(simplify(subs(subs(Gy_u_bb),Parameters,Values)),S);
Gy_d_bb_num = collect(simplify(subs(subs(Gy_d_bb),Parameters,Values)),S);

% Generate matlab transfer functions
% Small-Signal TF of Output voltage with respect to Duty cycle.
[symNum,symDen] = numden(Gy_d_bb_num(1,1));
TFnum = sym2poly(symNum);
TFden = sym2poly(symDen);
Gy1_d_tf = tf(TFnum,TFden);
Gvo_d_bb = Gy1_d_tf;
step(Gvo_d_bb)
pzmap(Gvo_d_bb)

% Small-Signal TF of Inductor Current with respect to Duty Cycle.
[symNum,symDen] = numden(Gy_d_bb_num(3,1));
TFnum = sym2poly(symNum);
TFden = sym2poly(symDen);
Gy3_d_tf = tf(TFnum,TFden);
Gil_d_bb = Gy3_d_tf;
step(Gil_d_bb)
pzmap(Gil_d_bb)
```

A.2: MATLAB Simulink Models

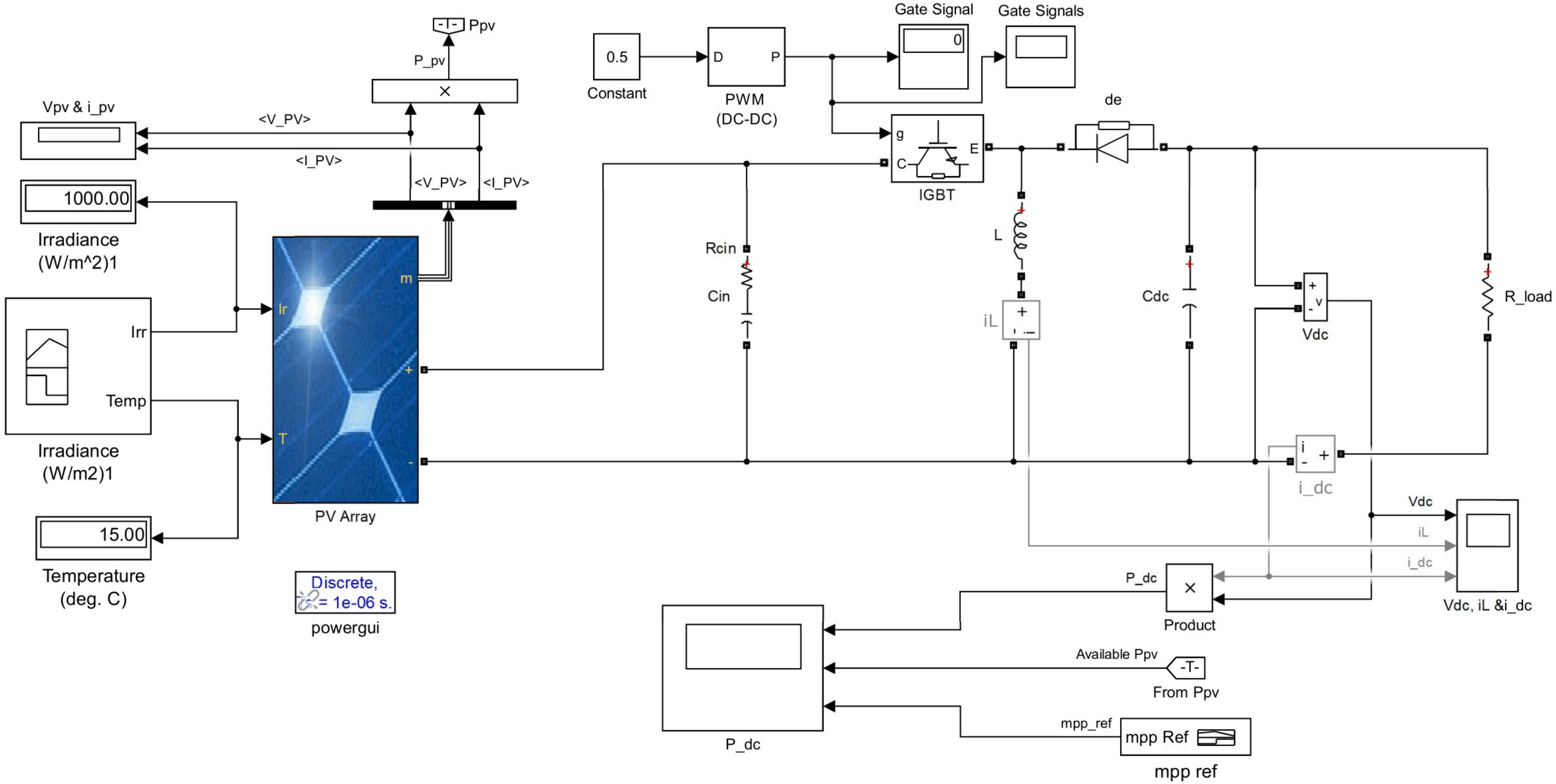

Figure A.1 Isolated DC stage under constant duty cycle operation

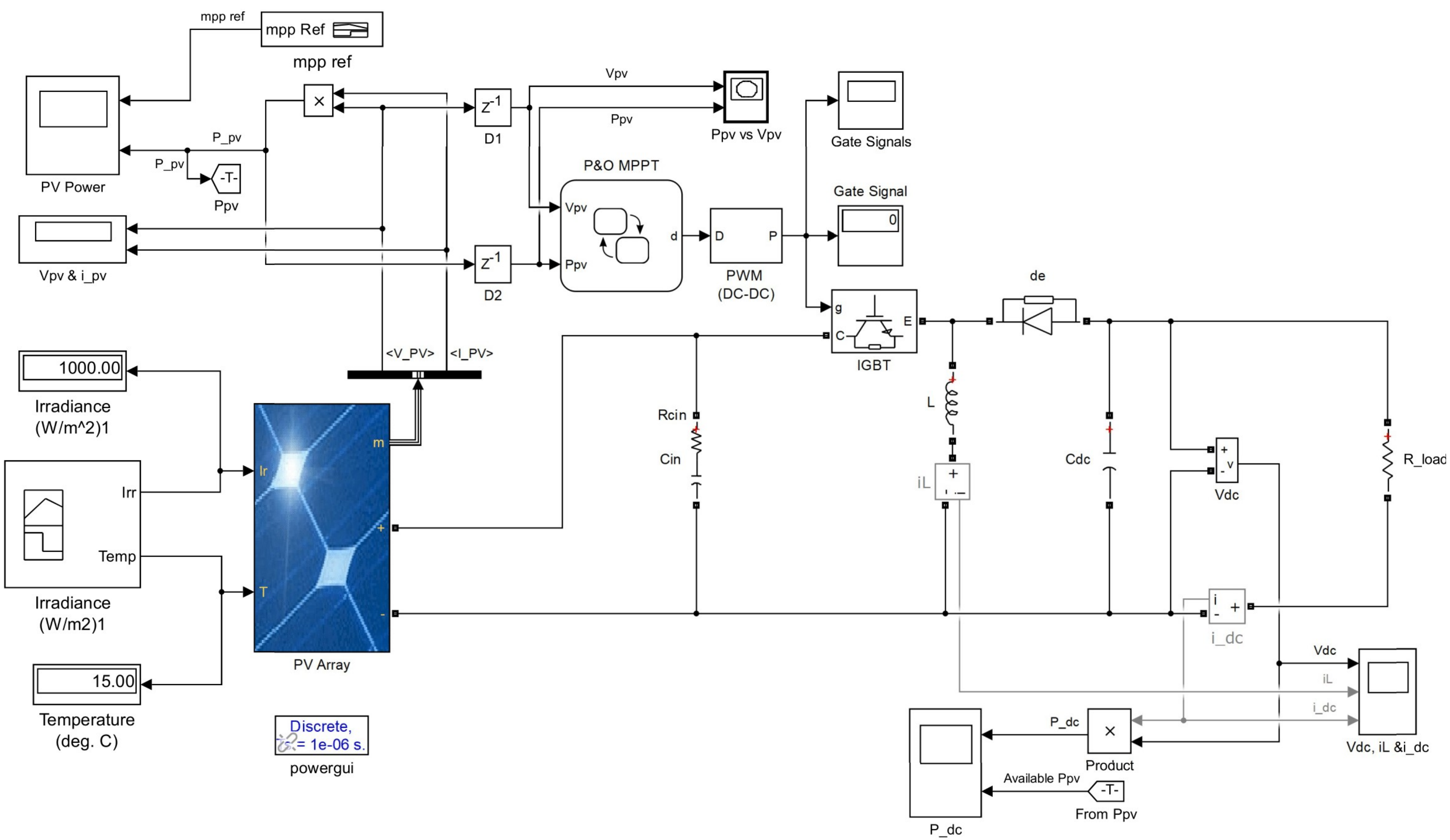

Figure A.2 P&O MPPT algorithm implementation in isolated DC system

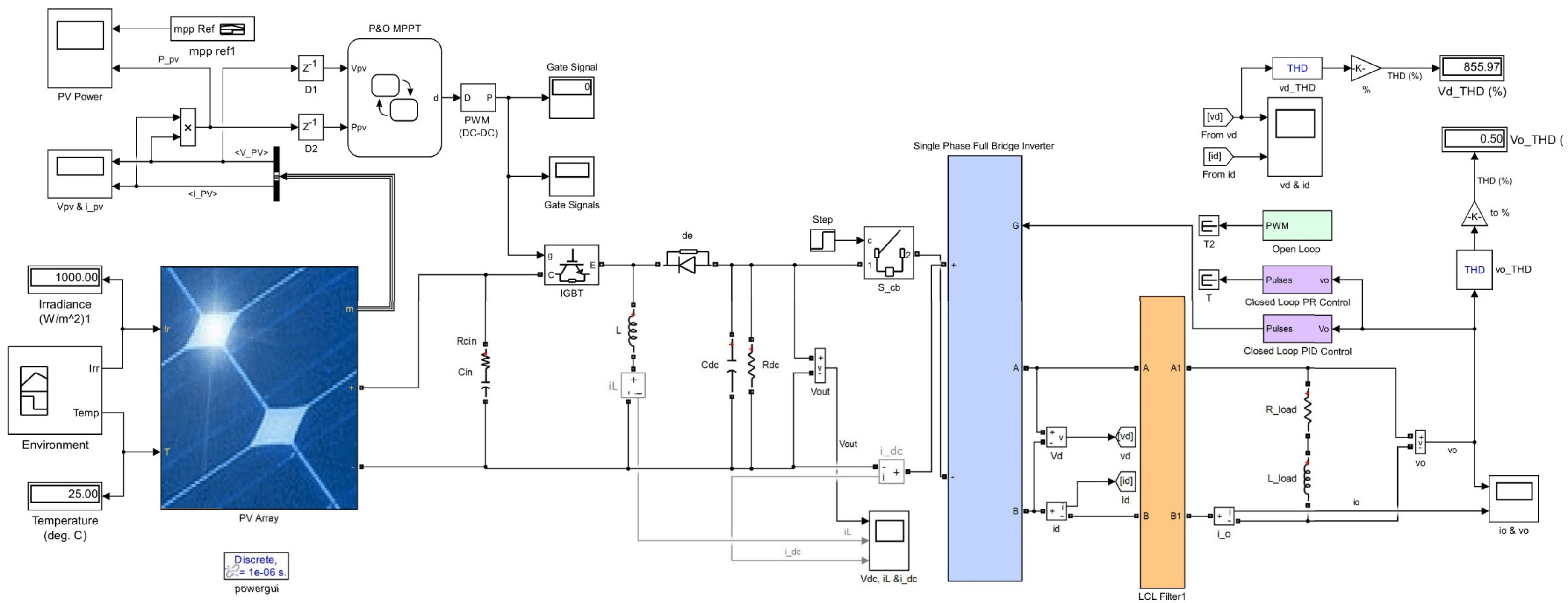

Figure A.3 Two-stage stage PV power system

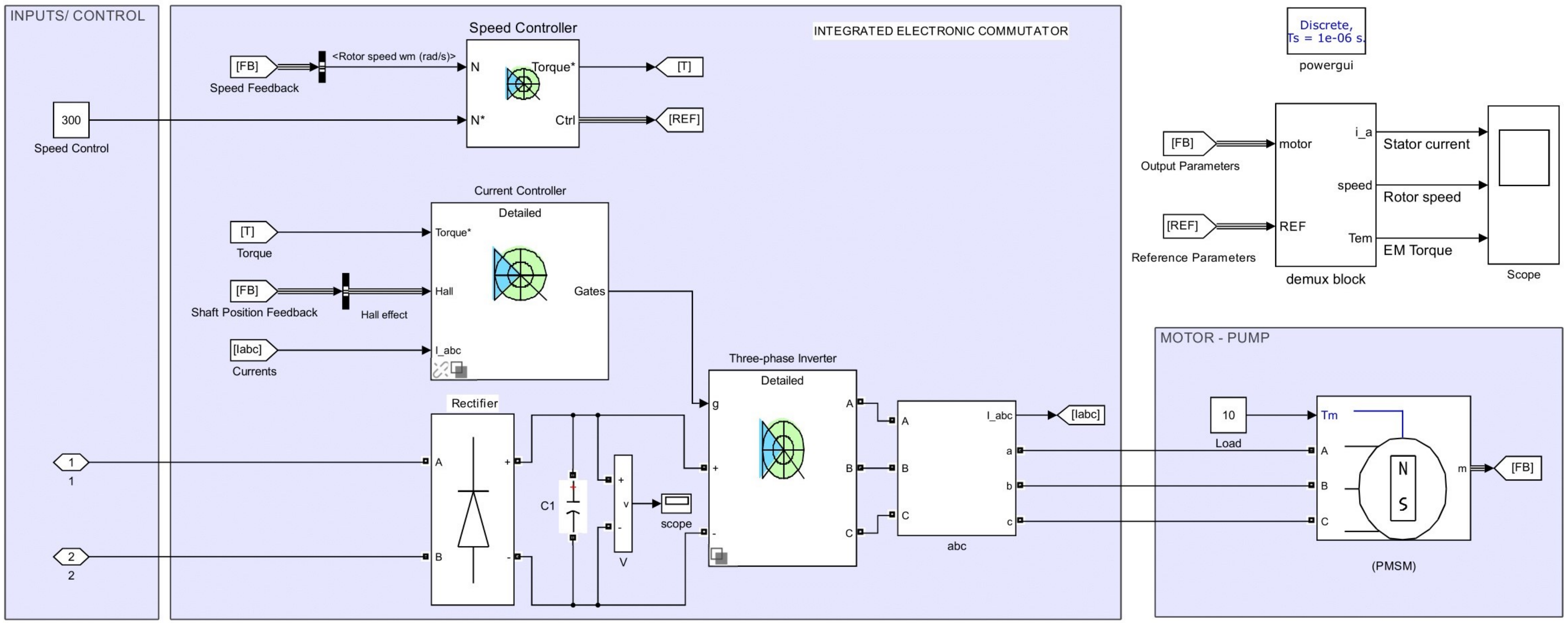

Figure A.4 Single-phase AC-input BLDC drive

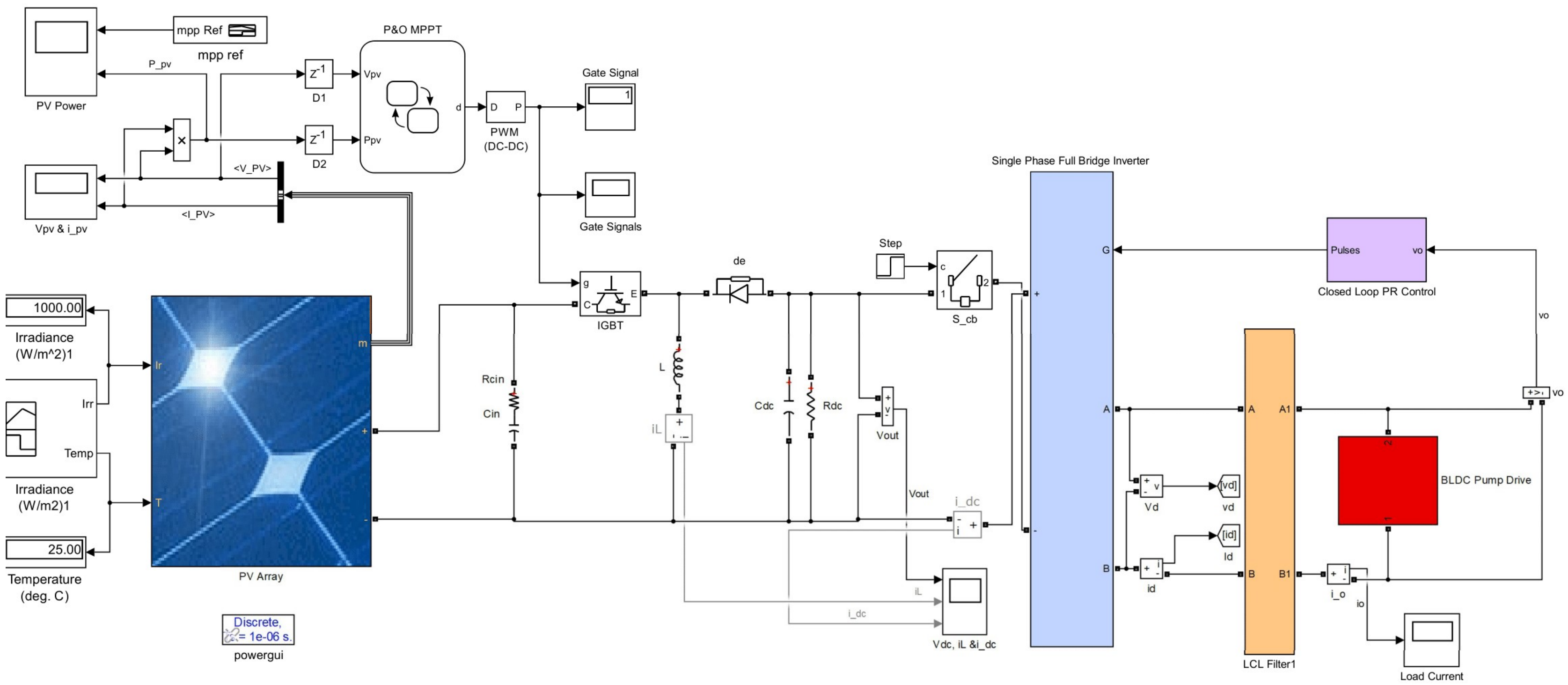

Figure A.5 Complete PV pumping system setup with BLDC drive